nature portfolio

https://doi.org/10.1038/s41560-022-01042-5

Supplementary information

Hydrogel protection strategy to stabilize water-splitting photoelectrodes

In the format provided by the authors and unedited

Supplementary Information for

Hydrogel Protection Strategy to Stabilise Water Splitting Photoelectrodes

Jeiwan Tan[1†], Byungjun Kang[2†], Kyungmin Kim[1], Donyoung Kang[2], Hyungsoo Lee[1], Sunihl Ma[1], Gyumin Jang[1], Hyungsuk Lee[2*], Jooho Moon[1*]

[1]Department of Materials Science and Engineering, Yonsei University, Seoul 03722, Republic of Korea

[2]School of Mechanical Engineering, Yonsei University, Seoul 03722, Republic of Korea

*Corresponding author. Correspondence should be addressed to H.L. (email: hyungsuk@yonsei.ac.kr) or to J.M. (email: jmoon@yonsei.ac.kr)
† These authors contributed equally to this work

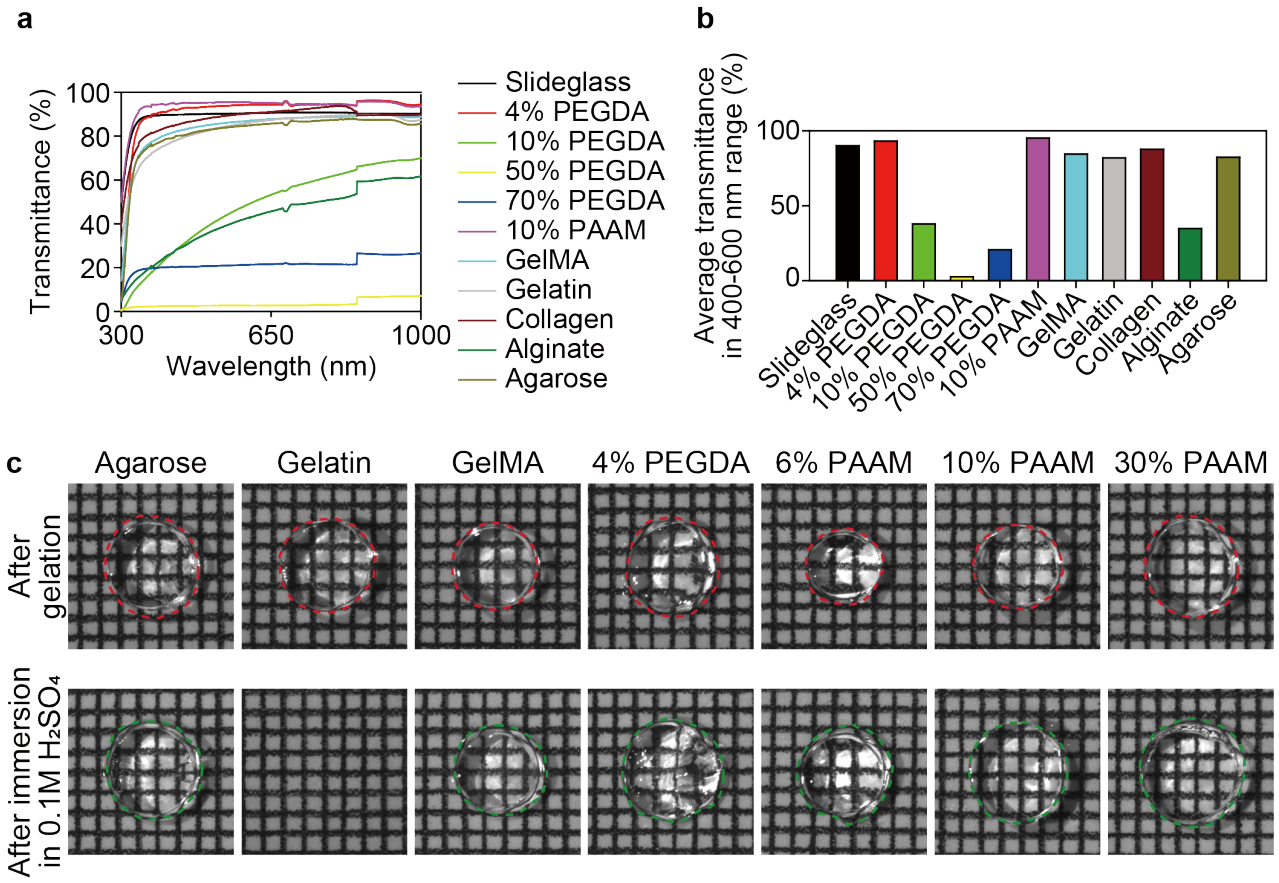

Supplementary Figure 1.
Screening of different hydrogel candidates prior to their application for PEC device protection. (a) Optical transmittance of hydrogels in a wavelength range of 300–1000 nm. All hydrogels are coated on a slide glass with a thickness of 400 µm. UV-visible spectroscopy is performed as soon as the sample is retrieved from a water bath. (b) Average optical transmittance of the hydrogels at 400–600 nm estimated from the data shown in (a). Agarose and GelMA exhibit low transmittance in the short-wavelength region. The transmittance of PEGDA decreases as a function of the monomer concentration, which renders it unsuitable for optimization. (c) Optical microscopic images of the hydrogels after gelation and immersion in a 0.1 M H_2SO_4 solution for 24 h. Red and green dotted lines represent the boundaries of the hydrogel after gelation and immersion in 0.1 M H_2SO_4 for 24 h, respectively. Gelatin is completely decomposed in H_2SO_4. Among various hydrogel candidates, PAAM exhibits the most desirable transmittance and chemical inertness.

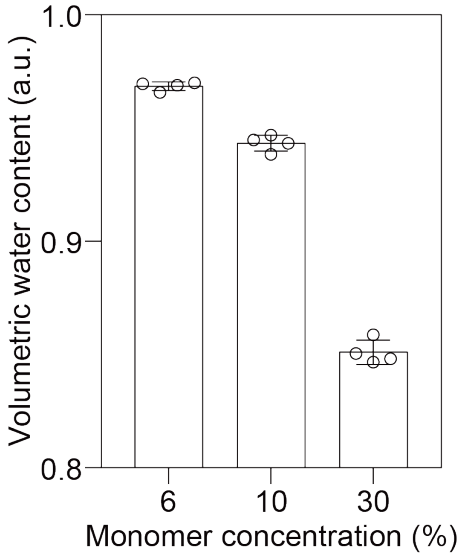

Supplementary Figure 2.
Volumetric water content of PAAM hydrogel at different monomer concentrations. Data are presented as mean ± standard deviation (n = 4 for each). The number of samples is four for each data point.

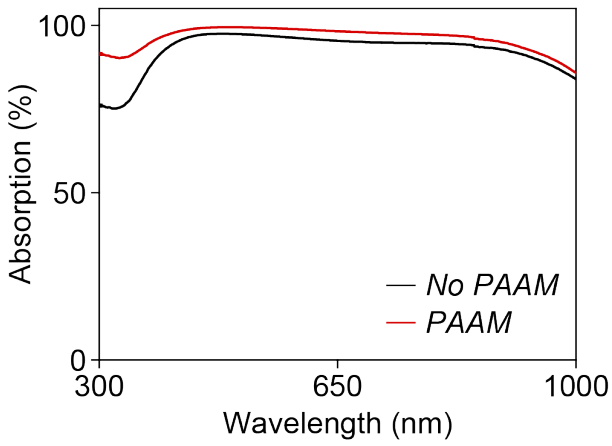

Supplementary Figure 3.
Optical effect of the hydrogel coating on the Sb_2Se_3 photocathode. Actual light absorption of the Sb_2Se_3 photocathodes, measured by subtracting the diffuse reflectance and transmittance from unity (no bubble condition). The increase in the light absorption over the entire wavelength range is ~2%.

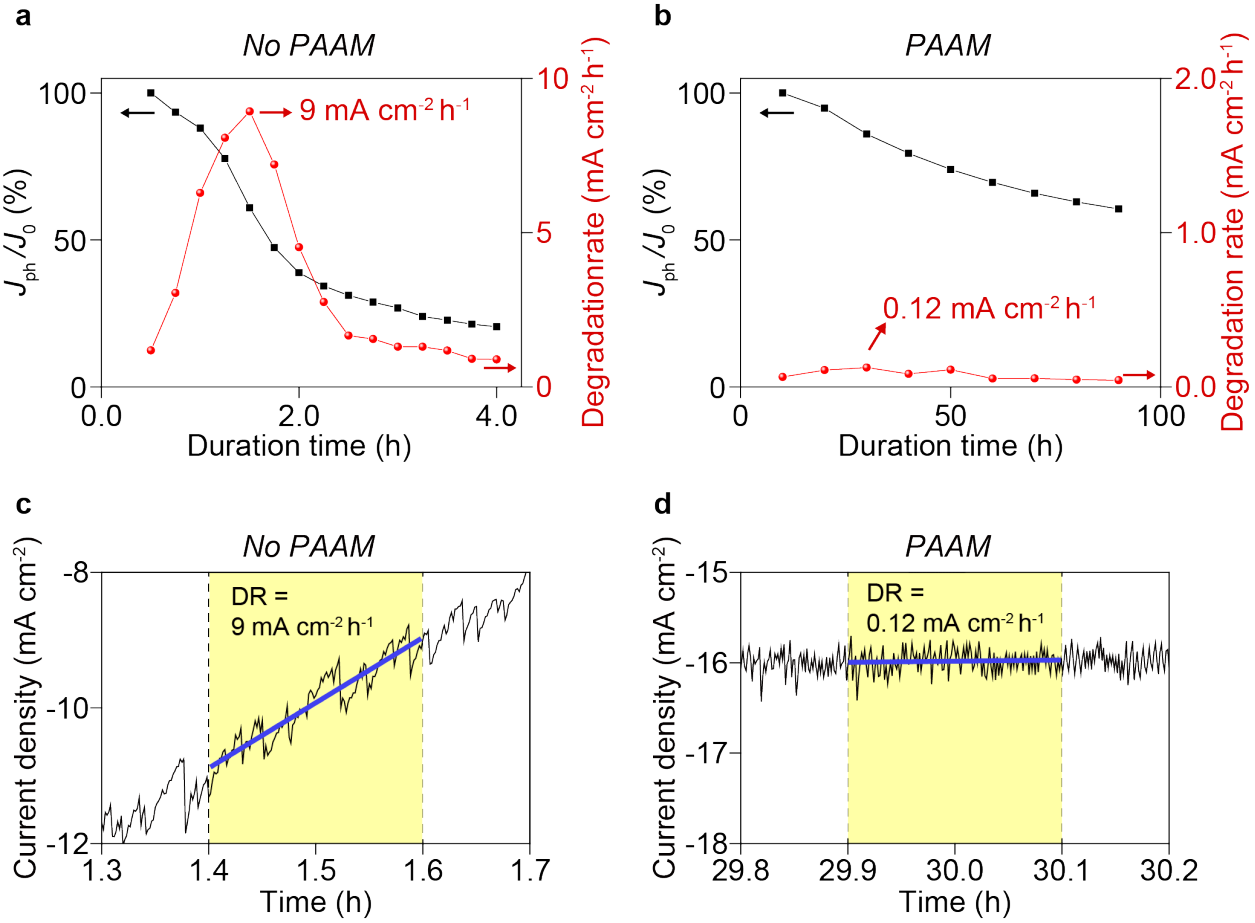

Supplementary Figure 4.
Degradation rate (DR) during the stability test of *No PAAM* and *PAAM*. The J_{ph}/J_o values and J_{ph} DR as a function of duration for (a) *No PAAM* and (b) *PAAM*. Representative examples of linear fitting to obtain the DR for (c) *No PAAM* and (d) *PAAM*.

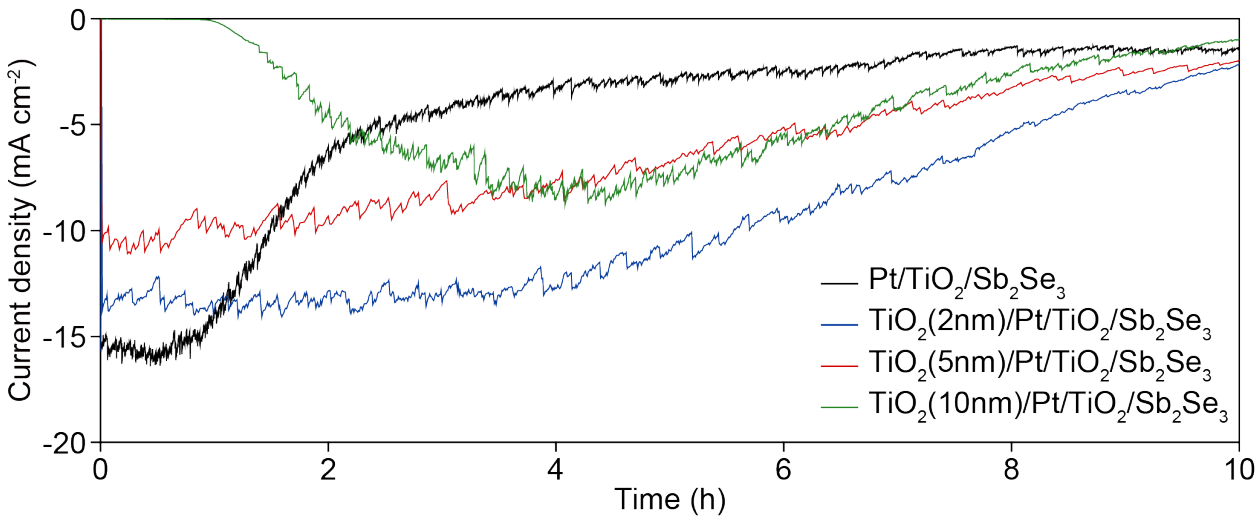

Supplementary Figure 5.
Photocurrent density–time curve of ALD-TiO_2/Pt/TiO_2/Sb_2Se_3 photocathodes as a function of the overlayer thickness (measured at 0 V_{RHE} in a pH 1 electrolyte). Although the stability is slightly enhanced when the ALD-TiO_2 overlayer is used compared to that without the overlayer, the initial photocurrent density decreases with the increase in the overlayer thickness. This observation suggests that coating the catalyst with a thin oxide overlayer slightly increases the stability compared to that of the non-protected counterpart. However, this strategy does not extent the device lifetime as much as the hydrogel protecting strategy (> 100 h).

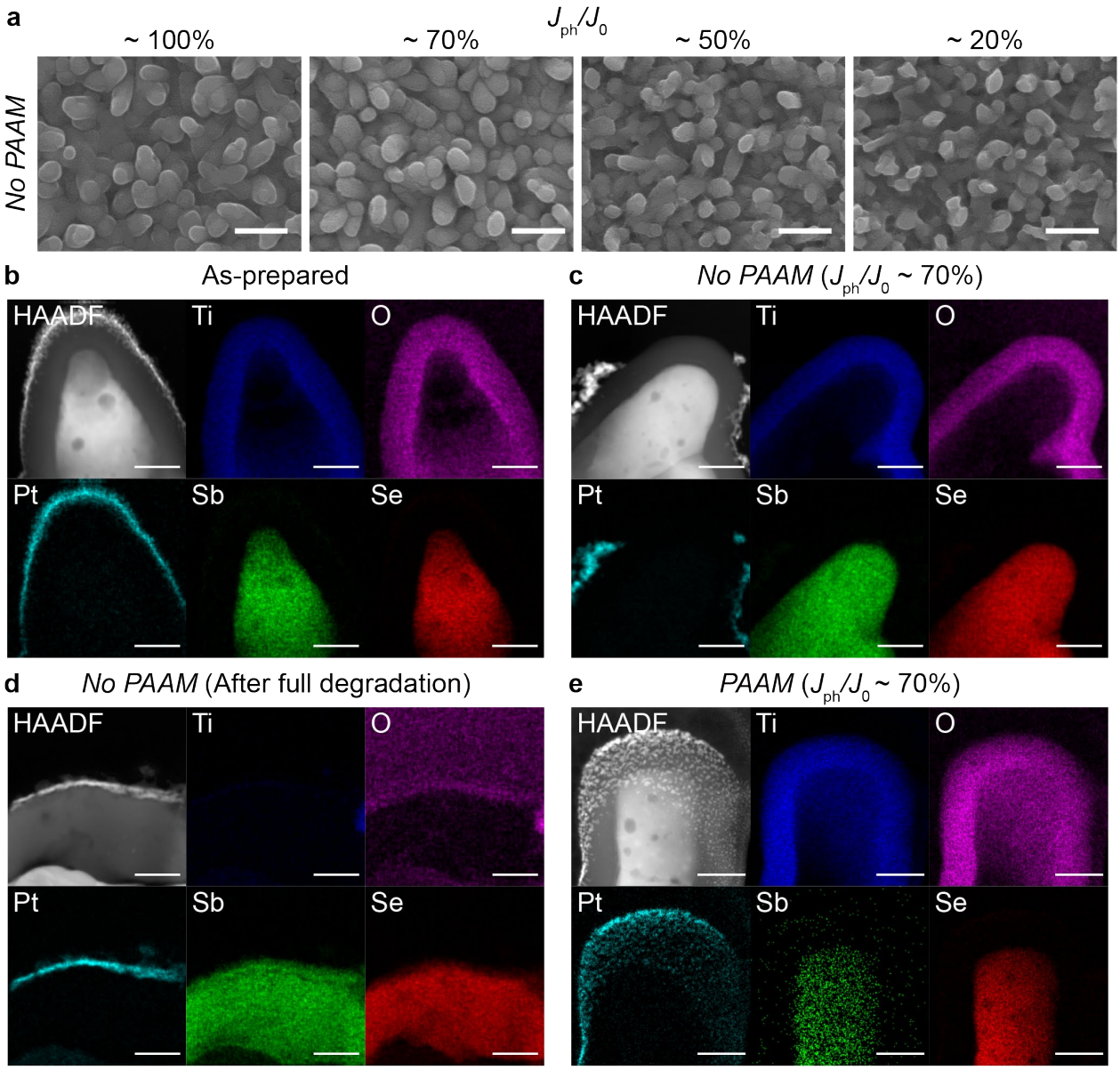

Supplementary Figure 6.
Morphological analysis of Sb_2Se_3 photocathodes. (a) Microstructural variations of *No PAAM* as a function of J_{ph}/J_o during the PEC operation. The scale bars represent 500 nm. High-angle annular dark-field imaging (HAADF) and STEM-EDS elemental mapping images of the cross-sections of the (b) as-prepared Sb_2Se_3 photocathode (*i.e., No PAAM* when J_{ph}/J_o is approximately 100%), (c) *No PAAM* when J_{ph}/J_o is approximately 70%, (d) *No PAAM* after full degradation, and (e) *PAAM* when J_{ph}/J_o is approximately 70% after ~100 h. The mapping images in (c) have been extracted from our previous study[7]. The scale bars represent 50 nm.

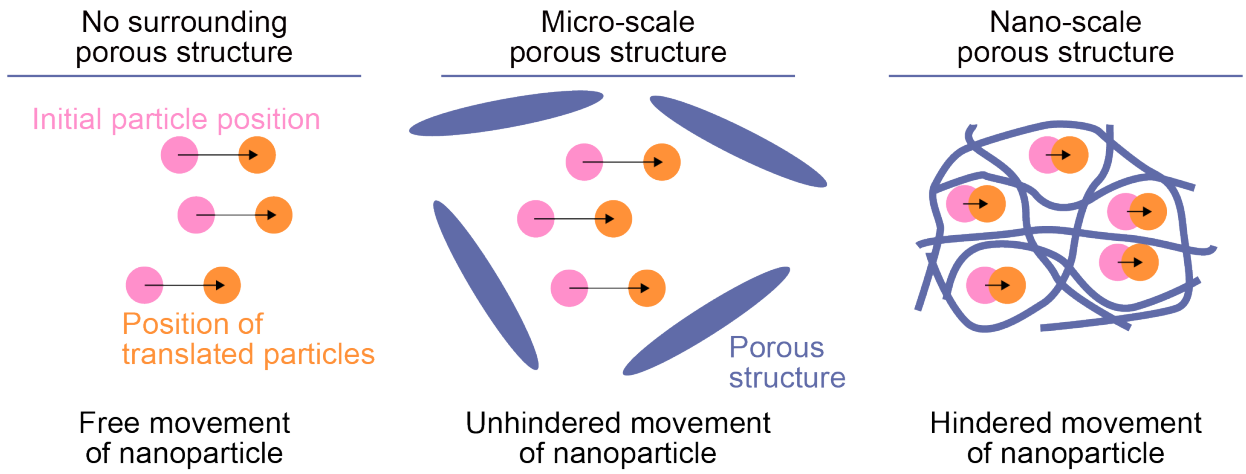

Supplementary Figure 7.
Schematic of the spatial confinement of Pt nanoparticles imposed by the microscale and nanoscale porous structures.

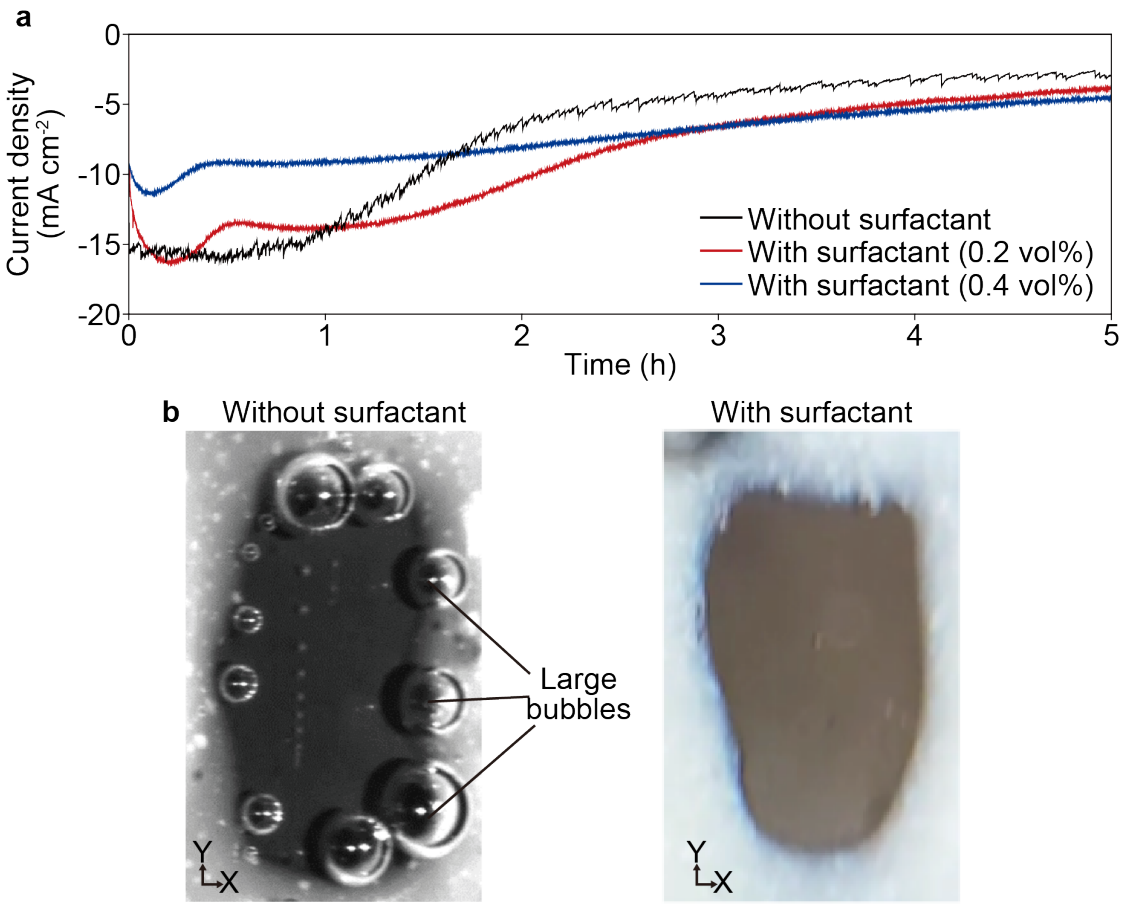

Supplementary Figure 8.
Stability test of Pt/TiO_2/Sb_2Se_3 (*No PAAM*) with and without a surfactant in the electrolyte. (a) Photocurrent–time curve and (b) photographs of *No PAAM* with and without the surfactant. The introduction of the surfactant in the electrolyte facilitates rapid bubble detachment and prevents the formation of large bubbles; however, this strategy does not enhance the device lifetime.

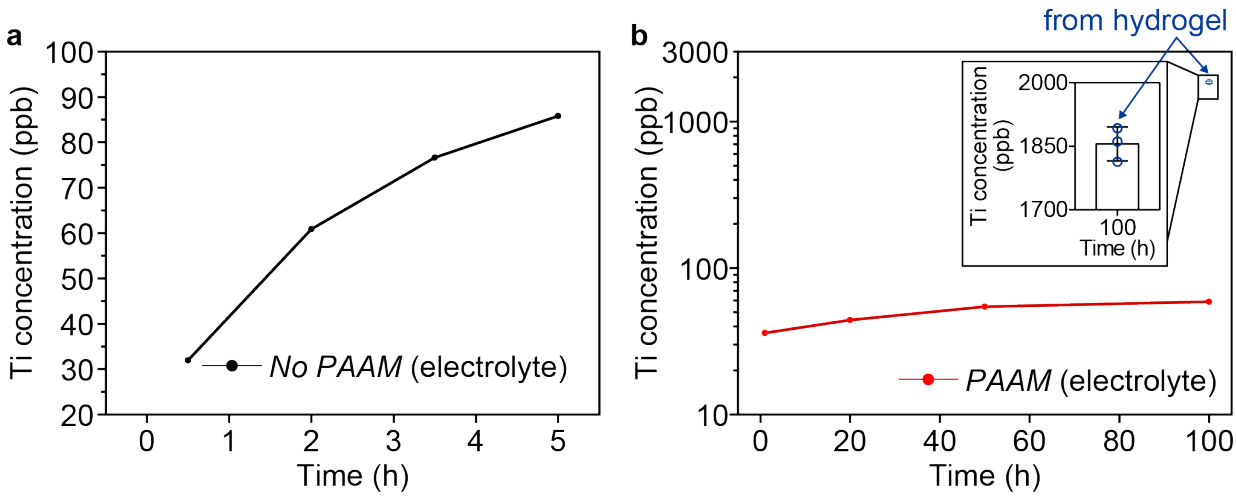

Supplementary Figure 9.

ICP-MS analysis of the electrolyte (0.1 M H_2SO_4) collected during the stability test. Change in the concentration of Ti as a function of time for (a) *No PAAM* and (b) *PAAM*. The Ti concentration increases for *No PAAM*, whereas the concentration for *PAAM* remains nearly unchanged. The Ti concentration for the mechanically detached hydrogel protector is ~30 times higher than that for the electrolyte counterpart after ~100 h. The concentrations of other elements (such as Pt, Sb, and Se) were below their detection limit. Data of '*PAAM* from hydrogel' were presented as mean ± standard deviation (n = 1 for '*No PAAM* (electrolyte)' and '*PAAM* (electrolyte)', and n = 3 for '*PAAM* from hydrogel').

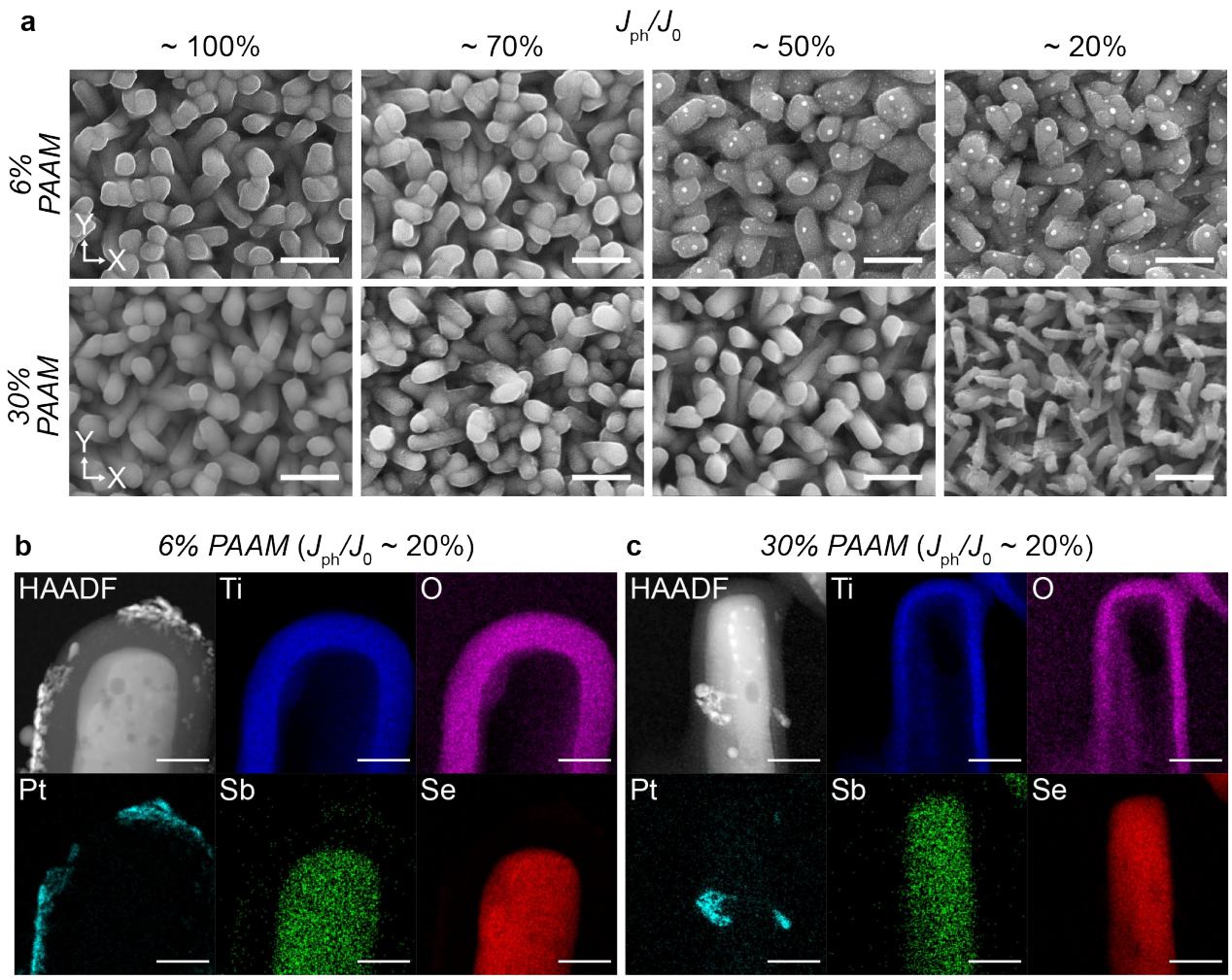

Supplementary Figure 10.
Morphological analysis of Sb_2Se_3 photocathodes in 6% and 30% *PAAM* with different monomer concentrations. (a) Variations in the surface morphologies of Sb_2Se_3 photocathodes. The hydrogel protector was mechanically pilled-off after operation. SEM images of the corresponding photocathodes were captured, with relative photocurrent ratios (J_{ph}/J_o) of 100%, 70%, 50%, and 20%. The scale bars represent 500 nm. Morphological analysis of the Sb_2Se_3 photocathodes with (b) 6% and (c) 30% *PAAM*. HAADF and STEM-EDS elemental mapping images of the cross-sections of 6% and 30% *PAAM,* captured when J_{ph}/J_o is approximately 20%. The scale bar represents 50 nm.

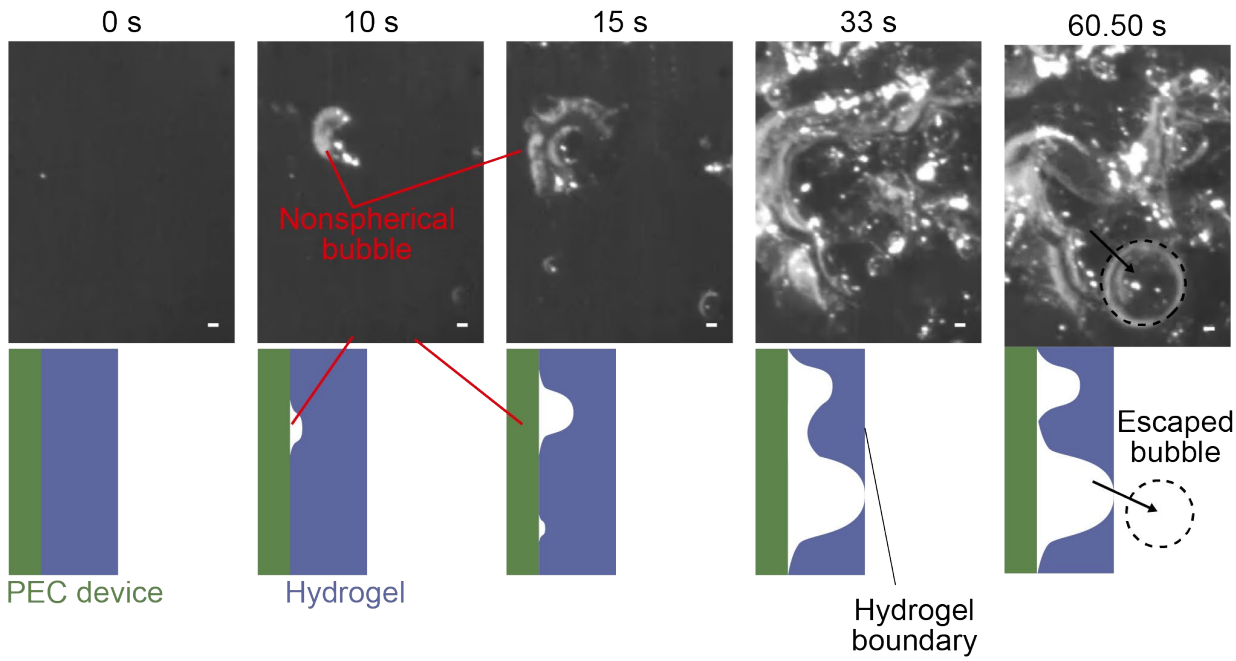

Supplementary Figure 11.
Magnified timelapse images and cross-sectional schematic of the fractured region of the hydrogel protector in 30% *PAAM*. The nonspherical bubble formed in the hydrogel indicates the fracture of the hydrogel[49,50]. The scale bars represent 100 μm.

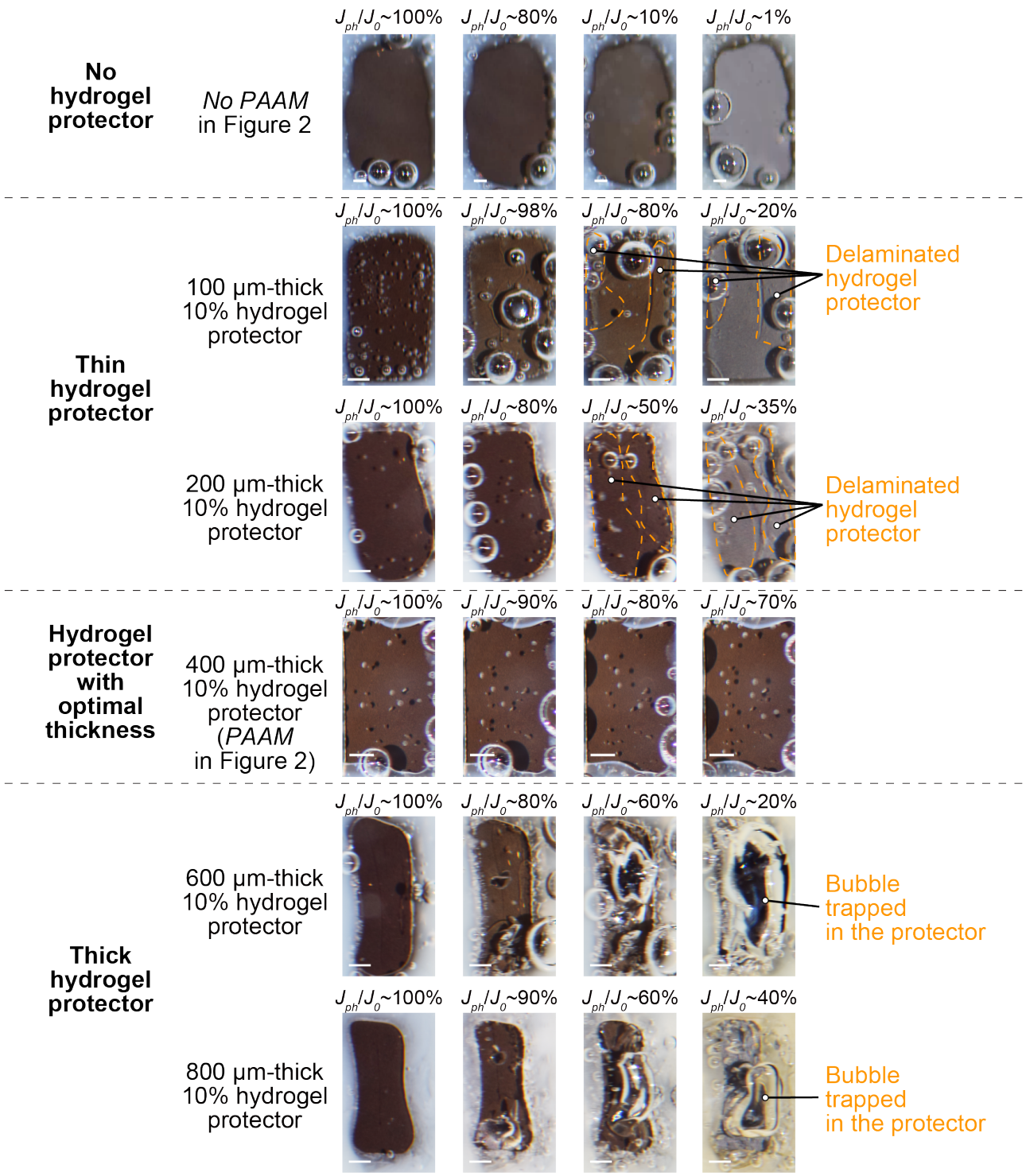

Supplementary Figure 12.
Representative photographs of *No PAAM* and *PAAM* with thicknesses of 100, 200 400, 600, and 800 µm during PEC operation. The photographs in Figures 5c, 6d, and 5e correspond to the 400-, 100-, and 800-µm-thick 10% hydrogel protectors, respectively. The scale bars represent 1 mm.

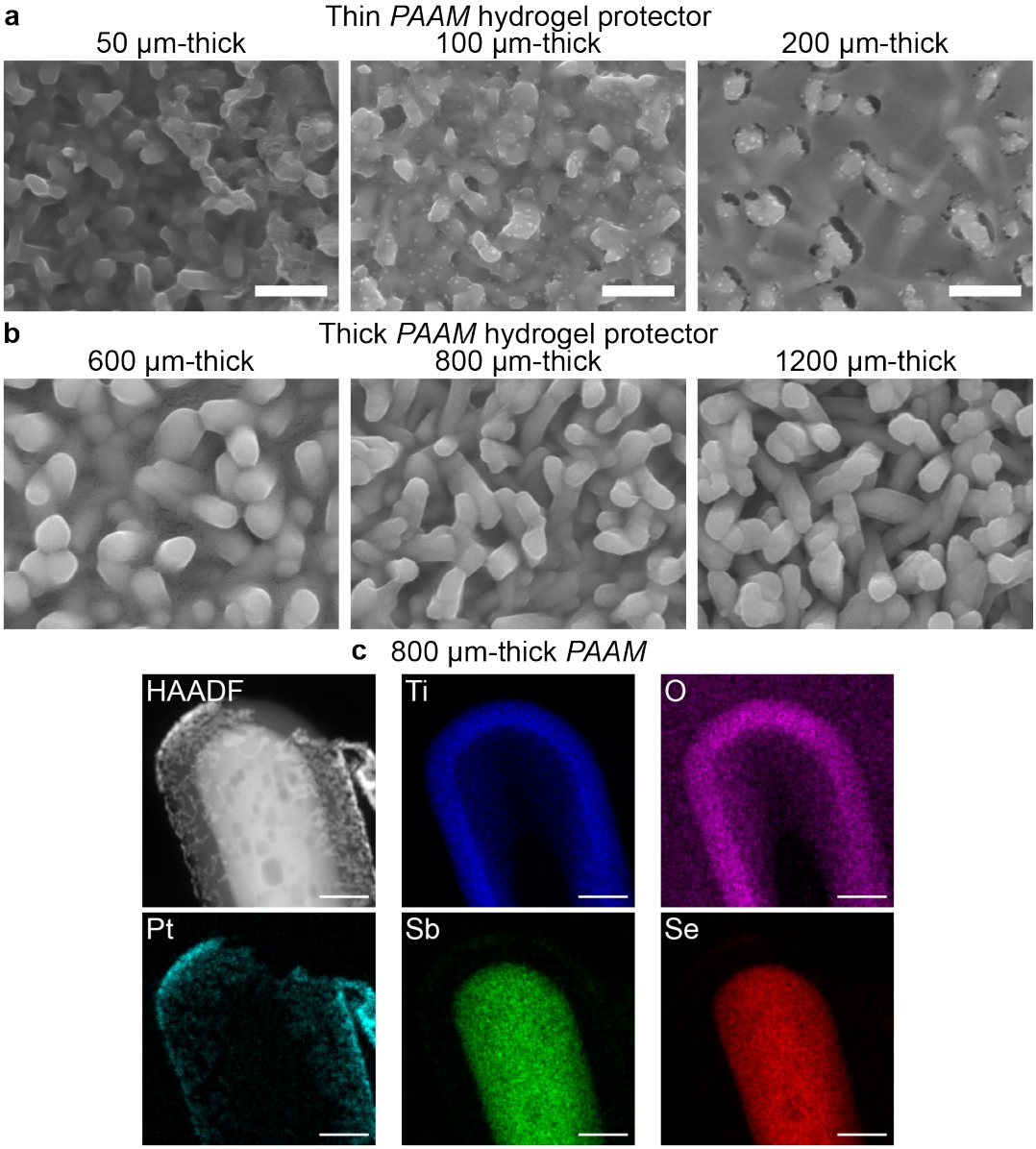

Supplementary Figure 13.
Morphological analysis of Sb_2Se_3 photocathodes with hydrogel protectors with different thicknesses. (a) Surface morphologies of Sb_2Se_3 photocathodes with thin PAAM hydrogel protectors (thicknesses of 50, 100, and 200 μm). (b) Surface morphologies of Sb_2Se_3 photocathodes with thick PAAM hydrogel protectors (thicknesses of 600, 800, and 1200 μm). The hydrogel protector is mechanically pilled-off after operation. SEM images correspond to the photocathodes when the relative photocurrent ratio (J_{ph}/J_o) is 20%. The scale bars represent 500 nm. The monomer concentration of the hydrogels is 10%. (c) HAADF and STEM-EDS elemental mapping images of the cross-sections of 800-μm-thick *PAAM,* captured when J_{ph}/J_o ~20%. The scale bars represent 50 nm. The monomer concentration of the hydrogels is 10%.

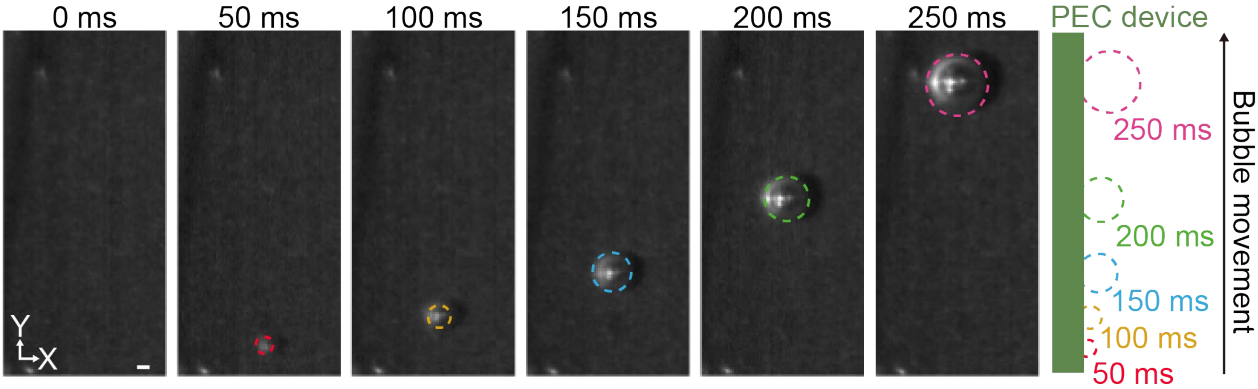

Supplementary Figure 14.
Nucleation, growth, and detachment of hydrogen bubbles for *No PAAM*. The dotted circles represent the bubbles at each time point. The bubble size immediately before the actual detachment (pink) is used for the statistics. The scale bar represents 100 μm.

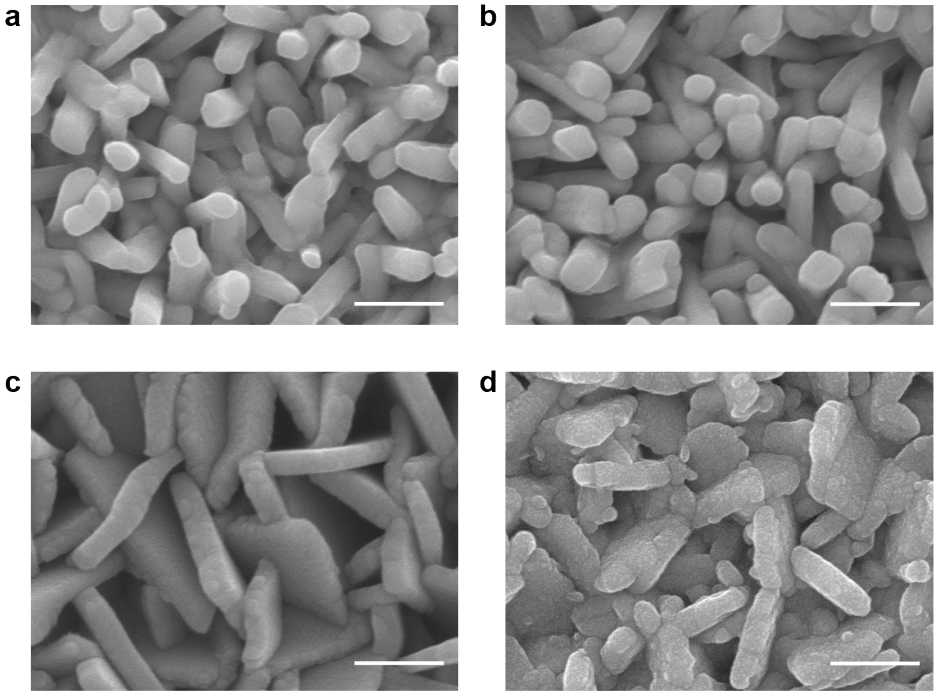

Supplementary Figure 15.
Morphological analysis of Sb_2Se_3 and SnS photocathodes for the electrolyte versatility test. Surface microstructures of the Sb_2Se_3 photocathodes after ~50 h of stability testing in (a) KPi electrolyte (pH 7) and (b) KBi electrolyte (pH 9). Surface microstructures of the (c) as-prepared SnS photocathodes (d) after ~50 h of stability testing in H_2SO_4 electrolyte (pH 1). The scale bars represent 500 nm.

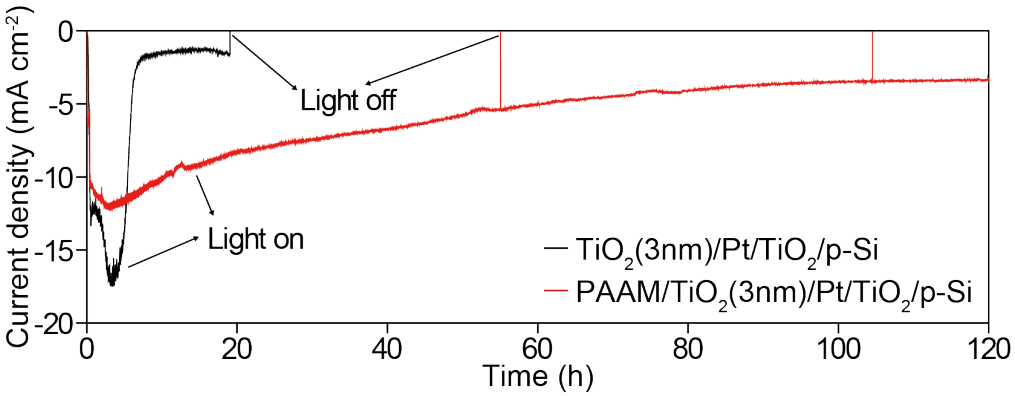

Supplementary Figure 16.
The stability of TiO_2(3nm)/Pt/TiO_2/p-Si with and without the hydrogel protector. Chronoamperometry was characterized at 0 V_{RHE} under acidic electrolyte (pH 1, H_2SO_4).

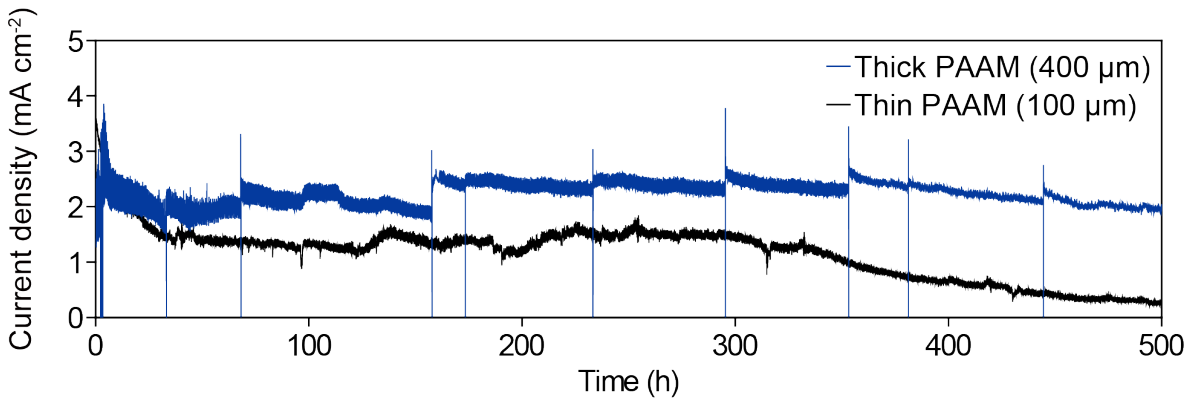

Supplementary Figure 17.
Stability testing of $NiFeO_x/BiVO_4$ photoanodes with 100-μm- and 400-μm-thick PAAM hydrogel protectors. The decrease in the initial J_{ph} to ~50% of the maximum J_{ph} in the first 30 h can be attributed to the trapping of bubbles inside the hydrogel protector. In the case of the 400-μm-thick PAAM, the photocurrent fluctuation for every light on/off results from the trapped bubbles inside the hydrogel. The trapped bubbles expand/contract when the production rate of O_2 gas is higher/lower than the rate of bubble escape. When the light is turned off, the O_2 production rate decreases and the trapped bubbles contract. When the light is turned on, because of the increased light absorption area, a temporally large current flows, followed by a decrease in the current magnitude as the trapped bubble expands again.

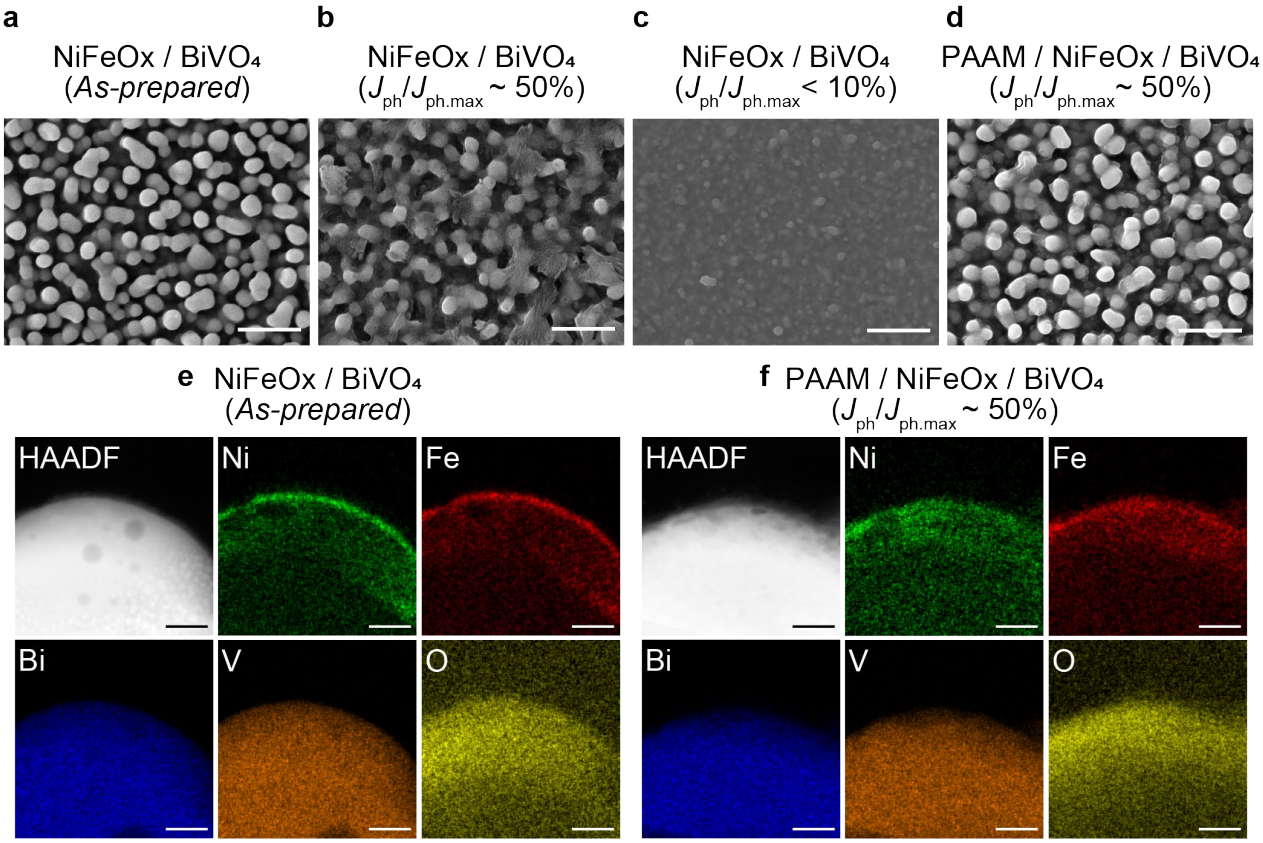

Supplementary Figure 18.

Morphological analysis of the $BiVO_4$ photoanodes. Surface microstructure variations of the $NiFeO_x/BiVO_4$ photoanode; (a) as-prepared state, (b) during PEC operation (J_{ph}/J_o ~50%), and (c) after almost full degradation (J_{ph}/J_o < 10%). (d) Surface microstructure of PAAM/$NiFeO_x/BiVO_4$ photoanode after 500 h (J_{ph}/J_o ~50%). The scale bars represent 1 μm. HAADF and STEM-EDS elemental mapping images of the cross-sections of the (e) $NiFeO_x/BiVO_4$ photoanode, and (f) PAAM/$NiFeO_x/BiVO_4$ photoanode after 500 h (J_{ph}/J_o ~50%). The scale bars represent 50 nm. The morphology of the $NiFeO_x/BiVO_4$ photoanode without the protector is significantly changed with photocurrent degradation, likely because of the dissolution of the constituent materials. In contrast, when the hydrogel protector is used, the surface morphology is nearly unchanged compared to that of the as-prepared $NiFeO_x/BiVO_4$ photoanode even after stability testing for 500 h.

Supplementary Note 1. Surface bubble size with and without hydrogel coating.

In the case of a superaerophobic hydrogel[1], the hydrogel coating enlarges the active sites during the PEC operation by suppressing the bubble growth along the device surface, rather than enhancing the catalytic activity. The active site density screened by bubbles grown along the device surface and dimension of the bubbles at detachment can affect the PEC efficiency (Supplementary Fig. 19).

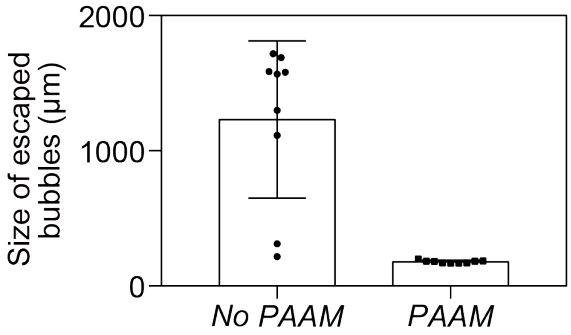

Supplementary Figure 19.
Size of escaped bubbles in *No PAAM* and *PAAM*. Data are presented as mean ± standard deviation (n = 10 for each). For statistics, the bubble size immediately before the actual detachment is considered for *PAAM* (Fig. 7) and *No PAAM* (Supplementary Fig. 14). The error bars represent the standard deviation.

Supplementary Note 2. Photocurrent fluctuation during stable operation of *PAAM*.

The current fluctuation is attributed to the repeated cycles of current reduction by bubble generation and current recovery by bubble detachment. We speculate three scenarios for the discontinuity points of the current, marked with black arrows in Supplementary Fig. 20.

1. (Scenario 1 for discontinuity point A) When relatively large bubbles are formed and detached at the edge of the devices, the decrease and recovery of photocurrent occur owing to light scattering by the bubbles.
2. (Scenario 2 for discontinuity point B) When the microsized gas bubbles formed inside the hydrogel protector merge and expand, the photocurrent suddenly decreases without an immediate current recovery.
3. (Scenario 3 for discontinuity point C) When the merged or expanded large bubble suddenly escapes, the photocurrent increases. This phenomenon is not directly influenced by the light chopping because a time delay of ~15 min exists after the light off/on.

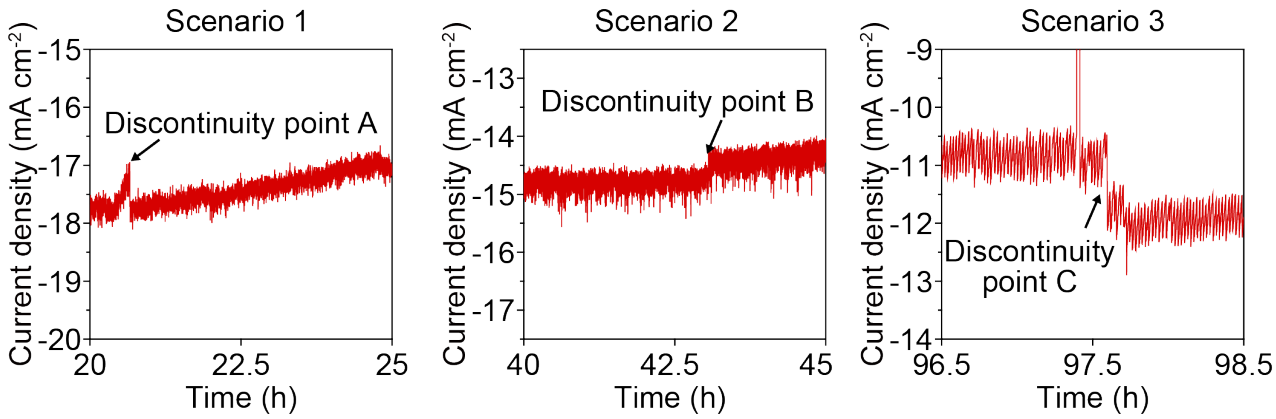

Supplementary Figure 20.
Locally magnified view of Figure 2d showing photocurrent fluctuations.

Despite the excellent protective role of the hydrogel, future work must be focused on achieving a semi-permanent device lifetime (*e.g.*, > 1000 h) through the engineering/functionalization of the hydrogel protector to allow more effective bubble escape without discontinuous behavior.

Supplementary Note 3. Image-based characterization of the thickness of TiO_2 layer.

The thickness of TiO_2 layer in Figure 4b was characterized by an image-based analysis (Supplementary Fig. 21a) using a software Fiji[2] (National Institutes of Health, Bethesda, MD, USA). First, the mapping data of Se and Ti layer were overlaid and the overlapping region between two layer was removed from the Ti mapping data. Then, the processed mapping data of Ti layer were straightened along the line drawn along the outer surface of Ti layer and then binarized. The thickness of Ti layer at each data point along the outer surface of Ti layer was measured from the straightened and binarized Ti mapping data (Supplementary Fig. 21b). The thickness of TiO_2 layer of *As-prepared*, *No PAAM*, and *PAAM* in Figure 4b was obtained from the STEM-EDS data in Supplementary Figure 6b, 6c, and 6e, respectively. The mean value of *As-prepared*, *No PAAM*, and *PAAM* in the graph of Supplementary 21b was presented as a bar graph in Figure 4b.

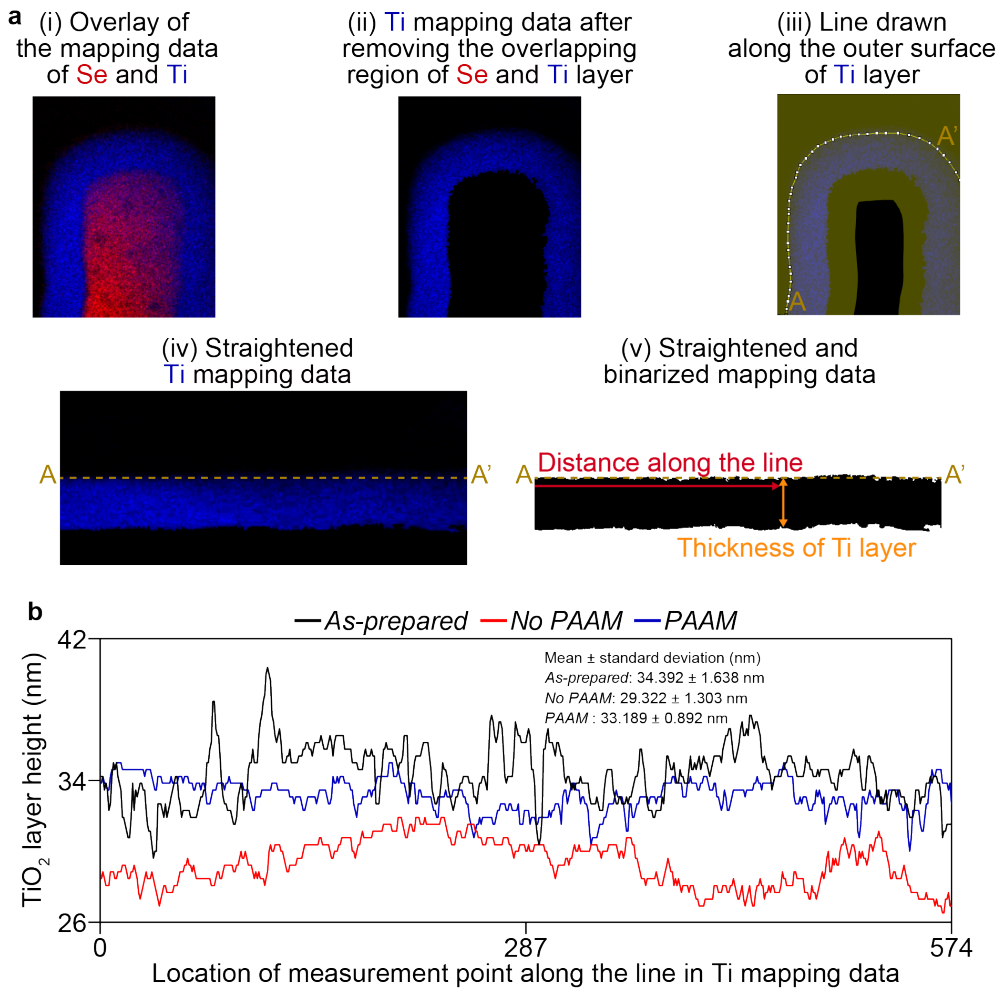

Supplementary Figure 21.
Image-based characterization of the thickness of TiO_2 layer. (a) Process of image-based analysis of TiO_2 layer from STEM-EDS mapping data. (b) Height profile along the line on the outer surface of Ti in the mapping data from Supplementary Fig. 6.

Supplementary Note 4. Theoretical analysis of TiO_2 dissolution rate with the device-on-top hydrogel protector.

The amount of $Ti(OH)_3$ on the TiO_2 surface does not significantly increase even during the continuous photoreduction of TiO_2[3]. This phenomenon indicates that the TiO_2 surface photoreduces into the $Ti(OH)_3$ species followed by its dissolution into the electrolyte, instead of remaining on the surface. We assume that all the $Ti(OH)_3$ species are dissolved into the electrolyte in the form of Ti^{3+} ions to simplify the calculation for mass conservation law (Supplementary Fig. 22a). We hypothesize that the device-on-top protector can decrease the surface dissolution rate of TiO_2 by controlling the 1) the boundary concentration of Ti^{3+} ions ($c_{boundary}$) and 2) diffusivity of Ti^{3+} ions inside the hydrogel (D_{gel}).

1-1. Factors affecting the boundary concentration

According to a theoretical study conducted by Scheiner and Hellmich[4], $c_{boundary}$ is saturated when the surface corrosion rate is an order of magnitude larger than the diffusion rate of the metal ions in the electrolyte. In this case, a thin salt film composed of metal ions appears at the solid surface, at which the saturation concentration of the dissolved metal ions ($c_{\mathrm{saturation}}$) is temporally and spatially constant. For convenience, we define the relative boundary concentration as $c_{\mathrm{relative}} = c_{\mathrm{boundary}}/c_{\mathrm{saturation}}$. $c_{\mathrm{relative}} = 0$ indicates that the surface corrosion is prevented, whereas $c_{\mathrm{relative}} = 1$ is suggestive of rapid surface corrosion.

With hydrogel protection, the boundary concentration can be decreased if the Pt agglomeration and detachment are prevented. For the theoretical calculations, c_{relative} is varied from 0.0 to 1.0.

1-2. Factors affecting the diffusivity of the Ti^{3+} ions inside the hydrogel

The diffusivity of the solute inside the hydrogel, D^{gel}, is lower than that in the solution, D^{solution}, because of steric and electrostatic interactions between the hydrogel network and solutes.[5-7] The relative diffusivity ($D_{\mathrm{relative}} = D_{\mathrm{gel}}/D_{\mathrm{solution}}$) of a metal ion in a typical polyacrylamide hydrogel is in the range 0.6–1.0,[6] which can be decreased owing to the small pore size and high electrostatic interaction between the solute and hydrogel[7]. In our calculations, the D_{relative} parameter varies from 0.0 to 1.0.

1-3. Theoretical calculation of the TiO_2 overlayer corrosion rate by using the mass conservation law

Considering the inertness of the Pt catalyst toward photocorrosion, the total mass change of the Ti^{3+} ions inside solid TiO_2 and the surrounding hydrogel domain is

$$\frac{\mathrm{d}M_{\mathrm{gel}}}{\mathrm{d}t} + \frac{\mathrm{d}M_{\mathrm{TiO_2}}}{\mathrm{d}t} = 0 \tag{1}$$

where $\frac{\mathrm{d}M_{\mathrm{gel}}}{\mathrm{d}t}$ and $\frac{\mathrm{d}M_{\mathrm{TiO_2}}}{\mathrm{d}t}$ are the mass-change rates of Ti^{3+} in the hydrogel and TiO_2 domains, respectively.

The mass flux of the TiO_2 domain varies only through the TiO_2–hydrogel interface, whose thickness changes with respect to time because of the TiO_2 dissolution; therefore, the mass-change rate in the TiO_2 domain is

$$\frac{\mathrm{d}M_{\mathrm{TiO_2}}}{\mathrm{d}t} = -\int_{A(t)} \overline{M} c_{\mathrm{Ti}} \mathbf{v}(\mathbf{x},t)\cdot\mathbf{n}(\mathbf{x},t)\,\mathrm{d}a \tag{2}$$

where $\overline{M}$, $\Lambda(t)$, c_{Ti}, $\mathbf{x}$, $\mathbf{v}(\mathbf{x},t)$, and $\mathbf{n}(\mathbf{x},t)$ represent the average molar mass of the TiO_2, TiO_2–hydrogel interface, Ti concentration in the TiO_2 domain, position and velocity vectors of the TiO_2–hydrogel interface, and normal vector, respectively. The equation of the mass-change rate in the TiO_2 domain is depicted in orange in Supplementary Fig. 22b.

As shown in Supplementary Fig. 22b, the mass change in the hydrogel domain includes the 1) mass change resulting from the concentration variation in the hydrogel domain (equation in white), 2) mass transport through the hydrogel–electrolyte interface (blue), and 3) mass transport through the TiO_2–hydrogel interface and mass change in the hydrogel domain caused by the movement of the TiO_2–hydrogel interface during the reductive dissolution of TiO_2 (magenta). Hence, the mass change rate in the hydrogel domain is

$$\begin{aligned}\frac{\mathrm{d}M_{\mathrm{gel}}}{\mathrm{d}t} &= \int_{\Omega_{\mathrm{gel}}} \overline{M}\frac{\partial c(\mathbf{x},t)}{\partial t}\mathrm{d}\Omega + \int_{\Gamma_{\mathrm{gel}}} \overline{M}\mathbf{J}(\mathbf{x},t)\cdot\mathbf{n}(\mathbf{x})\mathrm{d}a \\ &+ \int_{\Lambda(t)} \overline{M}\mathbf{J}(\mathbf{x},t)\cdot\mathbf{n}(\mathbf{x},t)\mathrm{d}a + \int_{\Lambda(t)} \overline{M}c_{\mathrm{boundary}}\mathbf{v}(\mathbf{x},t)\cdot\mathbf{n}(\mathbf{x},t)\mathrm{d}a\end{aligned} \tag{3}$$

where Ω_{gel}, Γ_{gel}, and $\mathbf{J}(\mathbf{x},t)$ represent the hydrogel domain, hydrogel-electrolyte interface, and mass flux through the interface, respectively.

Because $\int_{\Gamma}\mathbf{J}\cdot\mathbf{n}\mathrm{d}a = \int_{\Omega}\nabla\cdot\mathbf{J}\mathrm{d}\Omega$, according to Gauss' divergence theorem, Eq. 1 combined with Eqs. 2 and 3 can be expressed as

$$\int_{\Omega_{\mathrm{gel}}}\left(\frac{\partial c(\mathbf{x},t)}{\partial t}+\nabla\cdot\mathbf{J}(\mathbf{x},t)\right)\mathrm{d}\Omega+\int_{\Lambda(t)}\{\mathbf{J}(\mathbf{x},t)-(c_{\mathrm{Ti}}-c_{\mathrm{boundary}})\mathbf{v}(\mathbf{x},t)\}\cdot\mathbf{n}(\mathbf{x},t)\mathrm{d}a=0 \tag{4}$$

Because Eq. 4 holds for any domain and boundary,

$$\text{in } \Omega_{\mathrm{solution}}: \frac{\partial c(\mathbf{x},t)}{\partial t}+\nabla\cdot\mathbf{J}(\mathbf{x},t) = \frac{\partial c(\mathbf{x},t)}{\partial t}-\nabla\cdot(D_{\mathrm{gel}}\nabla c(\mathbf{x},t))=0 \tag{5}$$

$$\begin{aligned}\text{on } \Lambda(t): \{\mathbf{J}(\mathbf{x},t)-(c_{\mathrm{Ti}}-c_{\mathrm{boundary}})\mathbf{v}(\mathbf{x},t)\}\cdot\mathbf{n}(\mathbf{x},t)=\{-D_{\mathrm{gel}}\nabla c(\mathbf{x},t)-(c_{\mathrm{Ti}}-\\ c_{\mathrm{boundary}})\mathbf{v}(\mathbf{x},t)\}\cdot\mathbf{n}(\mathbf{x},t)=0\end{aligned} \tag{6}$$

where D_{gel} denotes the diffusivity of the solute in the hydrogel.

For the initial and boundary conditions

$$\text{in } \Omega_{\mathrm{solution}}\ (t=0): c = 0 \tag{7-1}$$

$$\text{on } \Gamma_{\mathrm{gel}}: c = 0 \tag{7-2}$$

$$\text{on } \Lambda(t\geq 0): c = c_{\mathrm{boundary}} \tag{7-3}$$

the solution for the one-dimensional case is

$$x_{\mathrm{d}}(t)=2\xi_{\mathrm{d}}\sqrt{D_{\mathrm{gel}}t} \tag{8}$$

where $x_{\mathrm{d}}(t)$ is the time-dependent position of the TiO_2–hydrogel interface, and ξ_{d} is a dimensionless parameter that can be obtained by solving

$$\frac{c_{\text{boundary}}}{c_{\text{Ti}}-c_{\text{boundary}}}e^{-\xi_d^2}=\sqrt{\pi}\xi_d\text{erf}(\xi_d) \tag{9}$$

c_{Ti} is obtained by multiplying the concentration of TiO_2 (3900 kg/m^3)[8] and 0.6 (*i.e.,* mass fraction of Ti in TiO_2). The diffusivity of a Ti^{3+} ion (D_{solution}) is set equal to the diffusivity of a Mn^{2+} ion (1.25×10^{-5}cm^2/s)[9] owing to their similar sizes. The saturation concentration ($c_{\text{saturation}}$) is 0.21 mol/L, which is the solubility of titanium hydroxides in a strongly acidic environment.[10]

The TiO_2 overlayer corrosion rate (R) is a function of D_{gel} and c_{boundary}.

$$R(D_{\text{relative}}, c_{\text{relative}}) =2\xi_d\sqrt{D_{\text{gel}}}=2\xi_d\sqrt{D_{\text{relative}}D_{\text{solution}}} \tag{10}$$

To demonstrate the variation in the TiO_2 overlayer corrosion rate as a function of the relative diffusivity and relative boundary concentration, the relative TiO_2 overlayer corrosion rate (R_{relative}) shown in Fig. 4c is calculated as

$$R_{\text{relative}}(D_{\text{relative}}, c_{\text{relative}}) =\frac{R(D_{\text{relative}}, c_{\text{relative}})}{R(D_{\text{relative}}=1, c_{\text{relative}}=1)} \tag{11}$$

where $R(D_{\text{relative}}=1, c_{\text{relative}}=1)$ can be considered as the corrosion rate for *No PAAM.*

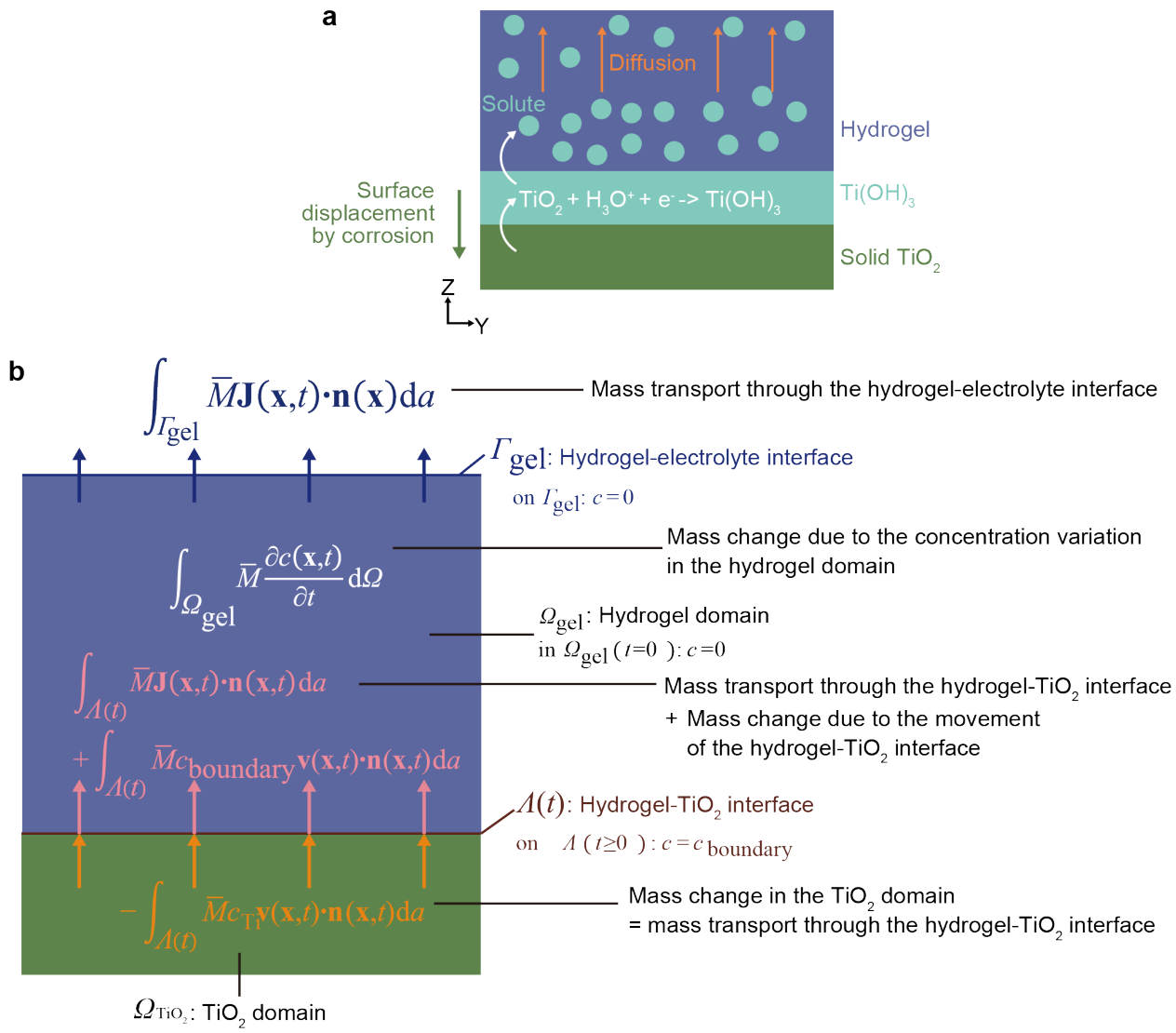

Supplementary Figure 22.
Theoretical analysis of the effect of the hydrogel protector on the TiO_2 surface corrosion. (a) Schematic of the mechanism of TiO_2 surface degradation on the PEC device. (b) Schematic of the mass conservation of the system with solid TiO_2 and hydrogel coated on the TiO_2 surface.

Supplementary Note 5. Theoretical analysis of the hydrogel fracture based on bubble growth.

Bubbles allow hydrogels to expand/contract in a reversible manner until irreversible deformation from hydrogel fracture occurs depending on the mechanical properties of the hydrogel[11,12]. Spherical or ellipsoidal bubbles are observed in the absence of hydrogel fractures, whereas nonspherical bubbles appear when the hydrogel is fractured[11,13]. In this study, we observe spherical or ellipsoidal bubbles in the cases of 6% and 10% *PAAM*, whereas small spherical bubbles and large nonspherical bubbles are observed in the case of 30% *PAAM*.

To understand the fracture mechanism in accordance with the bubble expansion, we perform further analysis using the theory developed by Kundu and Crosby[11]. The apparent pore size of the hydrogel is a few nanometers (Supplementary Fig. 23), considerably smaller than the bubble size ranging from a few micrometers to a few millimeters. Therefore, the hydrogel may act as a nonporous material for bubble expansion, and the deformation and fracture of the hydrogel from the bubble expansion can be analyzed based on continuum mechanics[11].

The pressure applied to the hydrogel during the bubble expansion is expected to increase and maximize in the early stage of bubble expansion. Thereafter, the pressure decreases when the bubble expands further. The maximum pressure applied to the hydrogel through bubble expansion ($P_{\max}$) can be predicted as

$$P_{\max} = \frac{5}{6}E + \frac{2\gamma}{r_s} \tag{12}$$

where r_s, E, and γ represent the radius of the initial defect, elastic modulus, and surface energy (=0.072 J/m^2)[11] of the hydrogel, respectively.

The critical pressure required for hydrogel fracture (P_f) can be predicted as

$$P_f = \left(\frac{\pi E G_c}{3}\right)^{0.5} \left(\frac{1}{r_s}\right)^{0.5} \tag{13}$$

where G_c is the critical energy-release rate of the hydrogel. When the pressure applied to the hydrogel exceeds the critical pressure, the bubble expansion results in hydrogel fracture.

Because $E \sim \phi^{2.3}$ and $G_c \sim \phi^{0.208}$, [11] where ϕ denotes the polymer volume fraction, $P_{\max}$ and P_f are proportional to $\phi^{2.3}$ and $\phi^{1.25}$, respectively, assuming that the hydrogel elasticity dominates the bubble expansion. Therefore, the ratio $P_{\max}/P_f$ increases with increase in ϕ of the hydrogel, which indicates that the hydrogel fracture is facilitated.

Because the initially nucleated bubble is considered as the initial defect, as reported in previous studies[14] the radius of the nucleated bubble is considered the radius of the initial defect. Moreover, the radius of the nucleated bubble is characterized as the radius of the circular and bright objects first observed at the site at which a large bubble is created (Supplementary Fig. 24a). The radii of the nucleated bubbles are approximately 30 μm (Supplementary Fig. 24b). Using these initial bubble radii and obtained polymer volume fraction of 6%, 10%, and 30% *PAAM* (Supplementary Fig. 23), $P_{\max}$, P_f (Supplementary Fig. 24c–f), and $P_{\max}/P_f$ (Fig. 6d) can be calculated. Only 30% *PAAM* corresponded to the region with $\frac{P_{\max}}{P_f} > 1$.

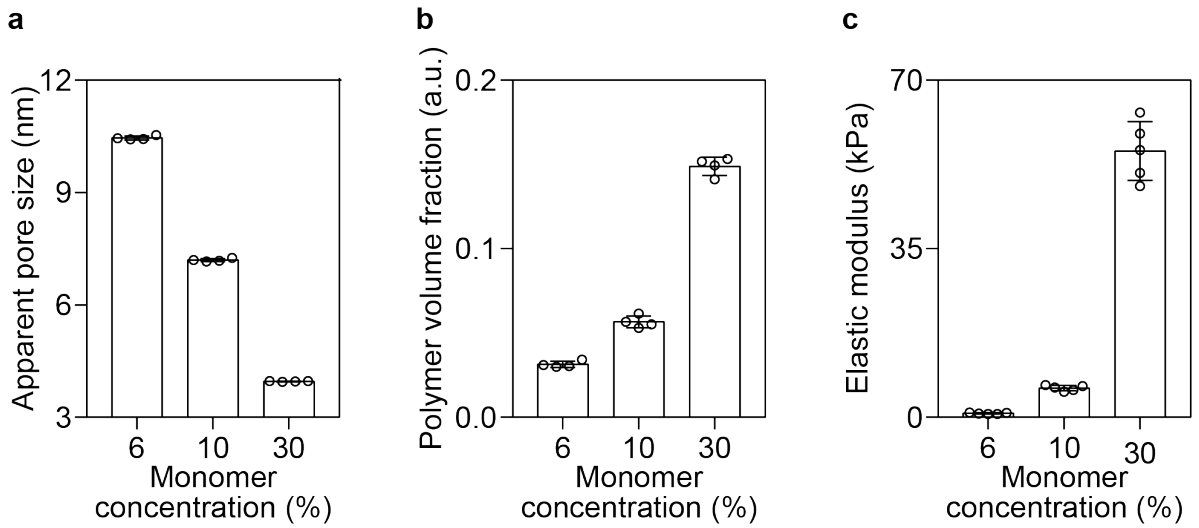

Supplementary Figure 23.

Effect of monomer concentration on the physical properties of the *PAAM* hydrogel. (a) Apparent pore size, (b) polymer volume fraction, and (c) elastic modulus of the *PAAM* hydrogel. Data are presented as mean ± standard deviation (n = 4 for each in (a) and (b), and n = 5 for each in (c)). With the increasing monomer concentration from 6% to 30%, the pore size and porosity decrease, whereas the polymer volume fraction and elastic modulus increase.

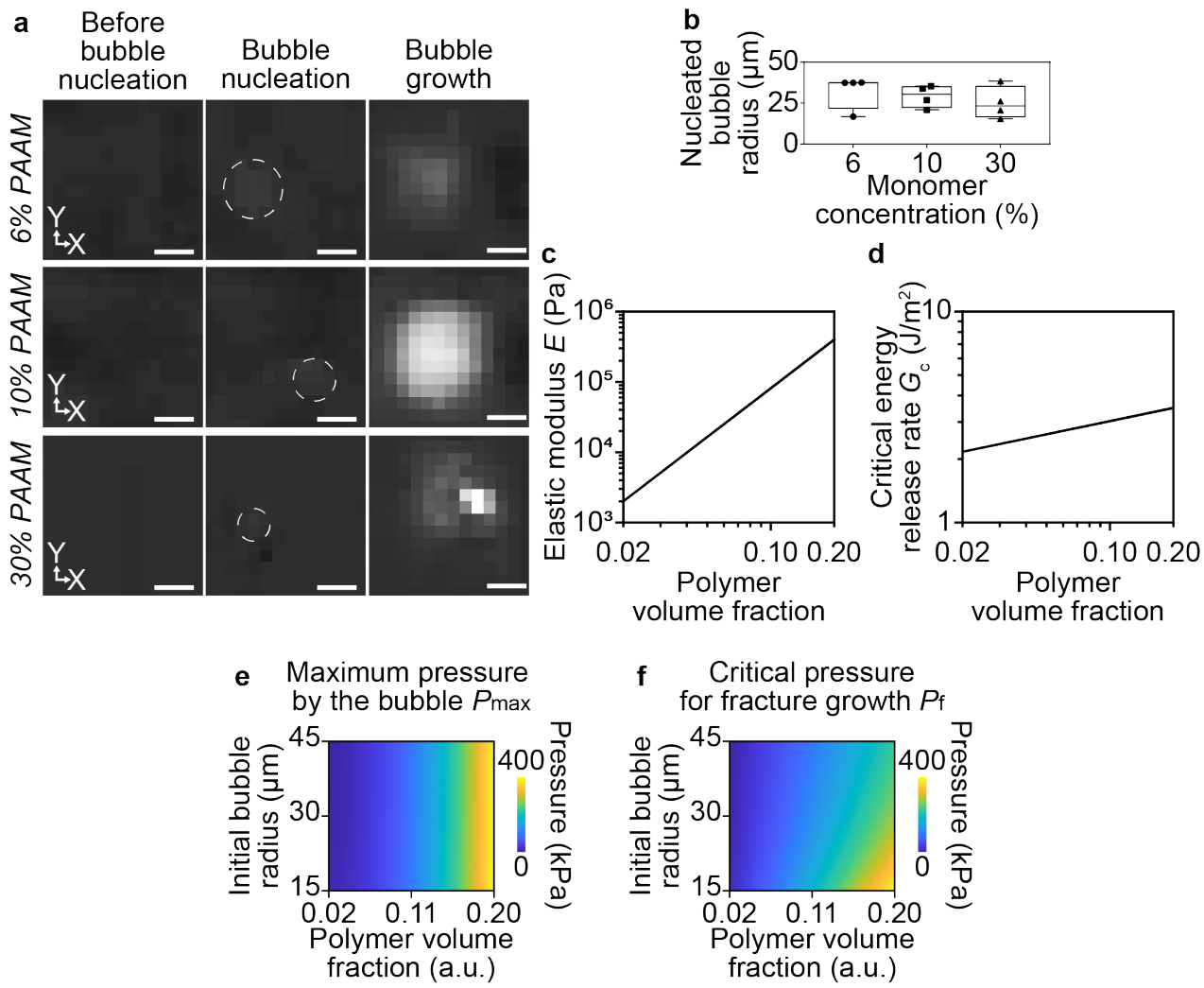

Supplementary Figure 24.

Theoretical analysis of hydrogel fracture induced by bubble expansion. (a, b) Image-based characterization of the initial bubble size. (a) Sequential images before, after, and during the bubble nucleation in the cases of 6%, 10%, and 30% *PAAM*. The scale bars represent 50 μm. (b) Radius of the nucleated bubble in 6%, 10%, and 30% *PAAM* devices. A bottom, centre, and top bound of the box represent the 25th, 50th and 75th percentiles, respectively (n = 4 for each). Whiskers of box represent the minima and maxima. (c–f) Theoretical analysis of the mechanics of the *PAAM* hydrogel, in which the bubble expands. (c) Elastic modulus (E) and (d) critical energy-release rate (G_c) of the hydrogel as a function of the polymer volume fraction (ϕ). (e) Maximum pressure applied on the hydrogel by the bubble (P_{max}) and (f) critical pressure to fracture the hydrogel (P_f) as a function of the polymer volume fraction and initial bubble radius. P_{max} and P_f are proportional to $\phi^{2.3}$ and $\phi^{1.25}$, respectively. The initial bubble radius does not significantly influence the magnitude of P_{max}.

Supplementary Note 6. Effect of post-annealing during the fabrication of Sb_2Se_3 nanostructured films.

The Sb_2Se_3 nanostructured film is fabricated via molecular ink-based spin coating and annealing process. Details of the fabrication procedure, including the optimized conditions of the Sb_2Se_3 molecular ink and relevant solution chemistry, as well as the general properties of the as-prepared Sb_2Se_3 nanostructured films have been presented in our previous report[15]. According to experimental observations, the post-annealing process at 200 °C for 30 min in air is important to ensure the PEC performance of the Sb_2Se_3 photocathodes (Supplementary Fig. 25). Without post-annealing, the J_{ph} and fill factor are significantly lower than those with annealing.

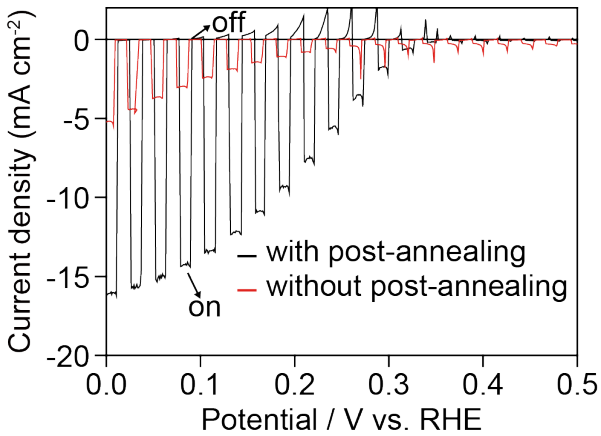

Supplementary Figure 25.
PEC characteristics of the Sb_2Se_3 photocathodes with and without the post-annealing process after spin coating.

The crystallinity and orientation of Sb_2Se_3 are maintained regardless of the post-annealing process, and no secondary phases are observed (Supplementary Fig. 26a). To clarify the effect of post annealing, we perform X-ray photoelectron spectroscopy (XPS) analysis of the Sb_2Se_3 film before and after the post-annealing (Supplementary Fig. 26b–d). All the XPS spectra are calibrated using the C 1s peak, which has a binding energy of 284.6 eV, and the background is fitted using the Shirley method. All the fitting curves are determined using a Gaussian peak function. After annealing, the Sb_2O_3 peak is dominantly observed in Sb 3*d* XPS spectra, whereas this peak is clearly reduced after surface etching for 100 s (Ar 500 eV; ~5 nm).

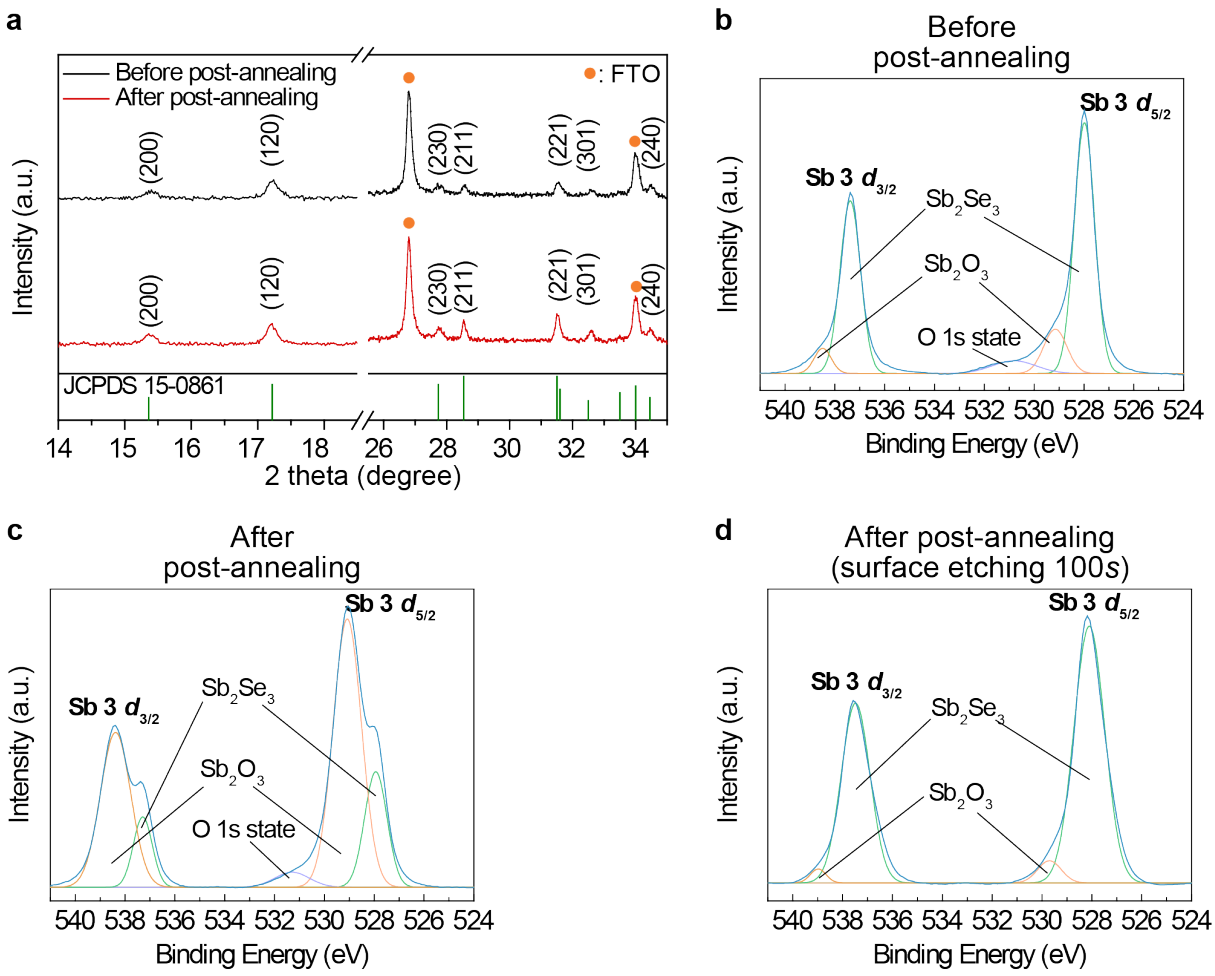

Supplementary Figure 26.
Surface properties of the as-prepared Sb_2Se_3 film before and after the post-annealing process. (a) X-ray diffraction (XRD) spectra of Sb_2Se_3 films before and after post-annealing. (b–d) XPS spectra of Sb 3*d* (a) before post-annealing, (b) after post-annealing, and (c) after post-annealing with surface etching for 100 s (Ar 500 eV, ~5 nm).

Supplementary Table 1. Summary of previously reported low-cost thin-film photocathodes

Device configuration (**catalysts are boldfaced**)	J_o [mA cm^{-2}]	Stability duration	J/J_0 after the stability duration	pH of electrolyte	Ref.
PAAM/**Pt**/TiO_2/Sb_2Se_3	19	100 h	70%	1	Present study
Pt/TiO_2/Sb_2Se_3	2	1 h	25%	1	16
Pt/TiO_2/Sb_2Se_3	12.5	2 h	60%	1	15
Pt/TiO_2/CdS/Sb_2Se_3	8.6	10 h	85%	6.5	17
Pt/C_{60}/TiO_2/Sb_2Se_3	17	10 h	95%	1	3
Pt/C_{60}/TiO_2/PABA/Sb_2Se_3	14	5 h	100%	1	18
RuO_x/TiO_2/Sb_2Se_3	10	2 h	100%	1	19
MoS_x/Sb_2Se_3	16	10 h	<10%	0	20
RuO_x/TiO_2/CdS/Sb_2Se_3	20	35	60%	6.25	21
Pt/TiO_2/AZO/Cu_2O	7.6	20 min	33%	5	22
Pt/TiO_2/AZO/Cu_2O	4.5	10 h	62%	5	23
Pt/TiO_2/AZO/Cu_2O	6	20 h	90%	5	24
Pt/TiO_2/Ga_2O_3/Cu_2O	2.95	2 h	60%	4.3	25
MoS_2/TiO_2/AZO/Cu_2O	5.7	5 h	33%*	1	26
RuO_2/TiO_2/AZO/Cu_2O	5	8 h	94%	5	27
RuO_x/TiO_2/AZO/Cu_2O	5.5	52 h	90%	5	24

RuO_x/TiO_2/Cu_2O	7	55 h	70%	5	28
RuO_x/TiO_2/AZO/Cu_2O/CuO:NiO	5.2	5 h	100%*	5	29
NiMo/TiO_2/Ga_2O_3/Cu_2O	6.3	100 h	~85%*	5	30
Pt/TiO_2/CdS/CZTS	~12*	1 h	75%	6.85	31
Pt/TiO_2/CdS/CBTSSe	12	10 h	100%	4.3	32
Pt/TiO_2/CdS/CBTSSe	4	4 h	67%	4.5	33
Pt–HfO_2/CdS/HfO_2/CZTS	14.6	24 h	100%	6.5	34
MoS_2/ITO/ZnO/CdS/CZTSe/ $MoSe_2$/Mo	10	2 h	100%	2	35
MoS_x/CdS/CZTS	5	10 h	100%	6.5	36
Pt/TiO_2/CdS/CuO	1.68	30 min	100%	7	37
RuO_x/TiO_2/CdS/Cu_2S	6	3.3 h	90%	5	38
Pt/TiO_2/CdS/SnS	19	2 h	100%	1	39

* The values were not specified in the relevant study and estimated from figures.

Supplementary Table 2. Summary of state-of-the-art Si photocathodes with matured development and record device stability.

Device configuration	J_o [mA cm^{-2}]	Stability duration	J/J_0 after the stability duration	pH of electrolyte	Ref.
SiO_x/Pt/SiO_2/p-Si	10	12 h	100%	1	40
Ir/TiO_2/F:SnO_2/Ti/pn$^+$-Si	35	24 h	<10%	14	41
Pt/TiO_2/pn$^+$-Si [(c)]	20	72 h	100%	0	42
Pt/Al_2O_3/pn$^+$ mc-Si [(a)]	27 (-0.8 V_{RHE})	100 h	100%	1	43
TiO_2/Pt/n$^+$p-Si [(c)]	10	168 h	100%	0	44
TiO_2/Pt/n$^+$np$^+$-Si [(c)]	~25	168 h	~95%*	0	45
GaN nanowire/GaN/pn-Si [(a)]	35	100 h	100%	1	46
MoS_2/Mo_xO/Mo_xSi/SiO_2/pn-Si [(c)]	11	60 d	100%	1	47
Pt/TiO_2/nc-Si:P/SiO_x/c-Si [(b,c)]	18	41 d	100%	1	48
p$^+$-InGaN/p^{++}-InGaN/n^{++}-InGaN/n$^+$-InGaN/pn-Si [(a,b)]	8	100 h	100%	1	49

*(a) = expensive and complicated fabrication process for surface nanostructuring/doping
*(b) = sophisticated device structure
*(c) = high temperature annealing

Supplementary Table 3. Monomer concentrations of 6%, 10%, and 30% *PAAM*.

Volume (μL)	Monomer concentration (%)		
	6%	10%	30%
DI water	888	817.4	464
100% AAm	65.2	108.6	326
2% Bis-acrylamide	40.8	68	204
10% AP	5	5	5
TEMED	1	1	1
Total	1000	1000	1000

Supplementary Table 4. Compositions of agarose and gelatin hydrogels.

	2% Agarose	10% Gelatin
Power (agarose or gelatin)	20 mg	100 mg
DI water	1000 μL	1000 μL
Total	1000 μL	1000 μL
Gelation	Incubation at 4 °C	

Supplementary Table 5. Compositions of 4%, 10%, 50%, and 70% PEGDA hydrogels.

	4% PEGDA with 0.05% Irgacure	70% PEGDA with 0.05% Irgacure	10% PEGDA with 0.1% Irgacure	50% PEGDA with 0.1% Irgacure
PEGDA solution (MW 575)	40 μL	700 μL	100 μL	500 μL
10% Irgacure 2959 solution (100 mg in 1 ml methanol)	5 μL	5 μL	10 μL	10 μL
DI water	955 μL	295 μL	890 μL	490 μL
Total	1000 μL	1000 μL	1000 μL	1000 μL
Gelation	UV illumination			

Supplementary Table 6. Composition of alginate hydrogels.

	6% Alginate with 0.2 M $CaCl_2$
10% Alginate solution (100 mg in 1 mL DI water)	600 µL
1 M $CaCl_2$ (1.47 g in 10 mL DI water)	200 µL
DI water	200 µL
Total	1000 µL
Gelation	The alginate solution is mixed with the $CaCl_2$ solution

Supplementary Table 7. Composition of collagen hydrogels.

	1 mg/mL collagen
Collagen I (3.52 mg/mL)	284 µL
10x PBS	100 µL
1 N NaOH	6.5 µL
DI water	609.5 µL
Total	1000 µL
Gelation	Incubation at 37 °C for 30 min

Supplementary Table 8. Composition of GelMA hydrogel.

	10% GelMA with 0.1% Irgacure
10% GelMA solution (100 mg in 1 mL 1x PBS)	990 µL
10% Irgacure 2959 solution (100 mg in 1 mL methanol)	10 µL
Total	1000 µL
Gelation	UV illumination

References for Supplementary Information

1. Jeon, D. *et al.* Superaerophobic hydrogels for enhanced electrochemical and photoelectrochemical hydrogen production. *Sci. Adv.* **6**, eaaz3944 (2020).
2. Schindelin, J. *et al.* Fiji: an open-source platform for biological-image analysis. *Nat. Methods* **9**, 676–682 (2012).
3. Tan, J. *et al.* Fullerene as a Photoelectron Transfer Promoter Enabling Stable TiO_2-Protected Sb_2Se_3 Photocathodes for Photo-Electrochemical Water Splitting. *Adv. Energy Mater.* **9**, 1900179 (2019).
4. Scheiner, S. & Hellmich, C. Stable pitting corrosion of stainless steel as diffusion-controlled dissolution process with a sharp moving electrode boundary. *Corros. Sci.* **49**, 319–346 (2007).
5. Tong, J. & Anderson, J. L. Partitioning and diffusion of proteins and linear polymers in polyacrylamide gels. *Biophys. J.* **70**, 1505–1513 (1996).
6. Shiva, A. H., Teasdale, P. R., Bennett, W. W. & Welsh, D. T. A systematic determination of diffusion coefficients of trace elements in open and restricted diffusive layers used by the diffusive gradients in a thin film technique. *Anal.Chim. Acta.* **888**, 146–154 (2015).
7. Amsden, B. Solute Diffusion within Hydrogels. Mechanisms and Models. *Macromolecules* **31**, 8382–8395 (1998).
8. PubChem. Titanium dioxide. https://pubchem.ncbi.nlm.nih.gov/compound/26042.
9. Krajewska, B. Diffusion of metal ions through gel chitosan membranes. *React. Funct. Polym.* **47**, 37–47 (2001).
10. Shkol'nikov, E. V. Thermodynamics of the dissolution of amorphous and polymorphic TiO2 modifications in acid and alkaline media. *Russian Journal of Physical Chemistry A* **90**, 567–571 (2016).
11. Kundu, S. & Crosby, A. J. Cavitation and fracture behavior of polyacrylamide hydrogels. *Soft Matter* **5**, 3963–3968 (2009).

12. Barney, C. W. *et al.* Cavitation in soft matter. *Proc. Natl. Acad. Sci. U.S.A.* **117**, 9157–9165 (2020).

13. Yang, S. *et al.* Hydraulic fracture geometry in ultrasoft polymer networks. *Int. J. Fract.* **219**, 89–99 (2019).

14. Movahed, P., Kreider, W., Maxwell, A. D., Hutchens, S. B. & Freund, J. B. Cavitation-induced damage of soft materials by focused ultrasound bursts: A fracture-based bubble dynamics model. *J. Acoust. Soc. Am.* **140**, 1374–1386 (2016).

15. Yang, W. *et al.* Adjusting the Anisotropy of 1D Sb_2Se_3 Nanostructures for Highly Efficient Photoelectrochemical Water Splitting. *Adv. Energy Mater.* **8**, 1702888 (2018).

16. Kim, J. *et al.* Self-oriented Sb_2Se_3 nanoneedle photocathodes for water splitting obtained by a simple spin-coating method. *J. Mater. Chem. A* **5**, 2180–2187 (2017).

17. Zhang, L. *et al.* Scalable Low-Band-Gap Sb2Se3 Thin-Film Photocathodes for Efficient Visible–Near-Infrared Solar Hydrogen Evolution. *ACS Nano* **11**, 12753–12763 (2017).

18. Tan, J. *et al.* Surface restoration of polycrystalline Sb2Se3 thin films by conjugated molecules enabling high-performance photocathodes for photoelectrochemical water splitting. *Appl. Catal. B* **286**, 119890 (2021).

19. Yang, W. *et al.* Time-Resolved Observations of Photo-Generated Charge-Carrier Dynamics in Sb2Se3 Photocathodes for Photoelectrochemical Water Splitting. *ACS Nano* **12**, 11088–11097 (2018).

20. Prabhakar, R. R. *et al.* Photocorrosion-resistant Sb2Se3 photocathodes with earth abundant MoSx hydrogen evolution catalyst. *J. Mater. Chem. A* **5**, 23139–23145 (2017).

21. Yang, W. *et al.* Benchmark performance of low-cost Sb_2Se_3 photocathodes for unassisted solar overall water splitting. *Nat. Commun.* **11**, 861 (2020).

22. Paracchino, A., Laporte, V., Sivula, K., Grätzel, M. & Thimsen, E. Highly active oxide photocathode for photoelectrochemical water reduction. *Nat. Mater*. **10**, 456–461 (2011).

23. Paracchino, A. *et al.* Ultrathin films on copper(I) oxide water splitting photocathodes: a study on performance and stability. *Energy Environ. Sci.* **5**, 8673–8681 (2012).

24. Azevedo, J. *et al.* On the stability enhancement of cuprous oxide water splitting photocathodes by low temperature steam annealing. *Energy Environ. Sci.* **7**, 4044–4052 (2014).

25. Li, C. *et al.* Positive onset potential and stability of Cu2O-based photocathodes in water splitting by atomic layer deposition of a Ga2O3 buffer layer. *Energy Environ. Sci.* **8**, 1493–1500 (2015).

26. Morales-Guio, C. G., Tilley, S. D., Vrubel, H., Grätzel, M. & Hu, X. Hydrogen evolution from a copper(I) oxide photocathode coated with an amorphous molybdenum sulphide catalyst. *Nat. Commun.* **5**, 3059 (2014).

27. Tilley, S. D., Schreier, M., Azevedo, J., Stefik, M. & Graetzel, M. Ruthenium Oxide Hydrogen Evolution Catalysis on Composite Cuprous Oxide Water-Splitting Photocathodes. *Adv. Funct. Mater.* **24**, 303–311 (2014).

28. Luo, J. *et al.* Cu2O Nanowire Photocathodes for Efficient and Durable Solar Water Splitting. *Nano Lett.* **16**, 1848–1857 (2016).

29. Son, M.-K. *et al.* A copper nickel mixed oxide hole selective layer for Au-free transparent cuprous oxide photocathodes. *Energy Environ. Sci.* **10**, 912–918 (2017).

30. Pan, L. *et al.* Boosting the performance of Cu2O photocathodes for unassisted solar water splitting devices. *Nat. Catal.* **1**, 412–420 (2018).

31. Yang, W. *et al.* Molecular Chemistry-Controlled Hybrid Ink-Derived Efficient Cu2ZnSnS4 Photocathodes for Photoelectrochemical Water Splitting. *ACS Energy Lett.* **1**, 1127–1136 (2016).

32. Zhou, Y. *et al.* Efficient and Stable Pt/TiO2/CdS/Cu2BaSn(S,Se)4 Photocathode for Water Electrolysis Applications. *ACS Energy Lett.* **3**, 177–183 (2018).

33. Song, J., Teymur, B., Zhou, Y., Ngaboyamahina, E. & Mitzi, D. B. Porous Cu2BaSn(S,Se)4 Film as a Photocathode Using Non-Toxic Solvent and a Ball-Milling Approach. *ACS Appl. Energy Mater.* **4**, 81–87 (2021).

34. Huang, D. *et al.* 3.17% efficient Cu2ZnSnS4–BiVO4 integrated tandem cell for standalone overall solar water splitting. *Energy Environ. Sci.* **14**, 1480–1489 (2021).

35. Grau, S. *et al.* Multi-layered photocathodes based on Cu 2 ZnSnSe 4 absorber and MoS 2 catalyst for the hydrogen evolution reaction. *J. Mater. Chem. A* **7**, 24320–24327 (2019).

36. Feng, K. *et al.* MoSx-CdS/Cu2ZnSnS4-based thin film photocathode for solar hydrogen evolution from water. *Appl. Catal. B* **268**, 118438 (2020).

37. Septina, W., Prabhakar, R. R., Wick, R., Moehl, T. & Tilley, S. D. Stabilized Solar Hydrogen Production with CuO/CdS Heterojunction Thin Film Photocathodes. *Chem. Mater.* **29**, 1735–1743 (2017).

38. Yu, Y.-X. *et al.* Solution-Processed Cu2S Photocathodes for Photoelectrochemical Water Splitting. *ACS Energy Lett.* **3**, 760–766 (2018).

39. Lee, H. *et al.* High-Performance Phase-Pure SnS Photocathodes for Photoelectrochemical Water Splitting Obtained via Molecular Ink-Derived Seed-Assisted Growth of Nanoplates. *ACS Appl. Mater. Interfaces* **12**, 15155–15166 (2020).

40. Labrador, N. Y. *et al.* Enhanced Performance of Si MIS Photocathodes Containing Oxide-Coated Nanoparticle Electrocatalysts. *Nano Lett.* **16**, 6452–6459 (2016).

41. Kast, M. G., Enman, L. J., Gurnon, N. J., Nadarajah, A. & Boettcher, S. W. Solution-Deposited F:SnO2/TiO2 as a Base-Stable Protective Layer and Antireflective Coating for Microtextured Buried-Junction H2-evolving Si Photocathodes. *ACS Appl. Mater. Interfaces* **6**, 22830–22837 (2014).

42. Seger, B. *et al.* Using TiO2 as a Conductive Protective Layer for Photocathodic H2 Evolution. *J. Am. Chem. Soc.* **135**, 1057–1064 (2013).

43. Fan, R. *et al.* Stable and efficient multi-crystalline n+p silicon photocathode for H2 production with pyramid-like surface nanostructure and thin Al2O3 protective layer. *Appl. Phys. Lett.* **106**, 013902 (2015).

44. Fan, R., Dong, W., Fang, L., Zheng, F. & Shen, M. More than 10% efficiency and one-week stability of Si photocathodes for water splitting by manipulating the loading of the Pt catalyst and TiO2 protective layer. *J. Mater. Chem. A* **5**, 18744–18751 (2017).

45. Yin, Z., Fan, R., Huang, G. & Shen, M. 11.5% efficiency of TiO2 protected and Pt catalyzed n+np+-Si photocathodes for photoelectrochemical water splitting: manipulating the Pt distribution and Pt/Si contact. *Chem. Commun.* **54**, 543–546 (2018).

46. Vanka, S. *et al.* High Efficiency Si Photocathode Protected by Multifunctional GaN Nanostructures. *Nano Lett.* **18**, 6530–6537 (2018).

47. King, L. A., Hellstern, T. R., Park, J., Sinclair, R. & Jaramillo, T. F. Highly Stable Molybdenum Disulfide Protected Silicon Photocathodes for Photoelectrochemical Water Splitting. *ACS Appl. Mater. Interfaces* **9**, 36792–36798 (2017).

48. Bae, D. *et al.* Carrier-selective p- and n-contacts for efficient and stable photocatalytic water reduction. *Catal. Today* **290**, 59–64 (2017).

49. Vanka, S. *et al.* InGaN/Si Double-Junction Photocathode for Unassisted Solar Water Splitting. *ACS Energy Lett.* **5**, 3741–3751 (2020).